Active fault scarps in southern Malawi and their implications for the distribution of strain in incipient continental rifts

L. N. J. Wedmore[1], J. Biggs[1], J. N. Williams[2], Å. Fagereng[2], Z. Dulanya[3], F. Mphepo[4], H. Mdala[4]

[1]Department of Earth Sciences, University of Bristol, UK.

[2]School of Earth and Ocean Sciences, Cardiff University, UK

[3]Geography and Earth Sciences Department, University of Malawi, Zomba, Malawi

[4]Geological Survey Department, Mzuzu Regional Office, Mzuzu, Malawi

Corresponding author: Luke Wedmore (luke.wedmore@bristol.ac.uk)

Key Points:

- We report 5 subparallel, previously unrecognised, active faults in the Zomba Graben, Malawi with 10-50 km long, 10-35 m high fault scarps
- Border faults are thought to dominate in incipient rifts, but we find intra-rift fault scarps accommodate 55 ± 24 % of extensional strain
- The Zomba Graben is a zone of relatively high seismic hazard linking Lake Malawi to the Urema Graben in Mozambique

Abstract

The distribution of deformation during the early stages of continental rifting is an important constraint on our understanding of continental breakup. Incipient rifting in East Africa has been considered to be dominated by slip along rift border faults, with a subsequent transition to focussed extension on axial segments in thinned crust and/or with active magmatism. Here, we study high-resolution satellite data of the Zomba Graben in southern Malawi, an amagmatic rift whose topography is dominated by the west-dipping Zomba fault. We document evidence for five sub-parallel fault scarps between 13 and 51 km long spaced ~10-15 km apart. The scarps consist of up to five segments between 4-18 km long, separated by minima in scarp height and river knickpoints. The maximum height of each fault scarp ranges from 9.5 ± 4.2 m to 35.3 ± 14.6 m, with the highest scarp measured on the intrabasin Chingale Step fault. We estimate that the scarps were formed by multiple earthquakes of up to M_w7.1, and represent a previously unrecognized seismic hazard. Our calculations show that 55 ± 24 % of extensional strain is accommodated across intrabasin faults within the ~50 km wide rift. This demonstrates that a significant proportion of displacement can occur on intrabasin faults during early stage rifting, even in thick continental lithosphere with no evidence for magmatic fluids.

Plain Language Summary

When continents begin to stretch, earthquakes occur on faults that incrementally accumulate slip to eventually form a rift valley. To estimate the hazard posed by these earthquakes, it is important to understand where these faults are located, and how much stretching they each accommodate. We analyse faults in the Zomba Graben, a young rift in southern Malawi, using high-resolution satellite data. Steep scarps indicate that recent

earthquakes have occurred at both the edges and in the middle of the rift valley. Pronounced activity in the rift middle is thought to require a thinned rigid outer layer of the Earth, or mechanically unfavourable faults at the rift edge. Neither of these factors have been observed in southern Malawi. We suggest that the distribution of active faults, and hence of earthquakes, is likely controlled by weaknesses in the middle and lower parts of the Earth's crust.

1. Introduction

The development and interaction of faults dominate deformation in the early stages of continental rifting and contribute to the eventual breakup of continental lithosphere (Cowie et al. 2005; Ebinger and Scholz, 2012). Numerical models of the early phase of continental rifting and non-volcanic rifted margins suggest that faults grow in isolation and are distributed across a region of extension (Heimpel and Olson, 1996; Cowie 1998; Cowie et al., 2000; Huismans and Beaumont, 2007; 2014; Brune, 2014). Because of changes in sedimentation, displacement rates, fault geometry, volcanism, and rift extension direction that can occur during later phases of continental extension (Gawthorpe and Leeder, 2001; Cowie et al., 2000; Buck, 2004; Ebinger, 2005; Brune, 2014; Philippon et al., 2015), patterns of distributed faulting generated during these early stages of rifting are commonly obscured. Consequently, there are also conceptual models, especially those based on the East African Rift System, which suggest that early stage rifting (first ~10 Ma) is dominated by activity on border faults (Ebinger, 2005; Corti, 2009). Observations from Lake Tanganyika suggest that up to 90% of early-rift extensional strain is accommodated on border faults (Muirhead et al., 2019) and that intrabasin faulting is limited to small-displacement faults that accommodate flexure (Turcotte and Schubert, 1982). After this stage of dominantly

64 localised strain across the rift border faults, strain is expected to migrate to the rift interior
65 when the lithosphere is weakened by magmatic intrusions (Buck, 2004; Kendall et al., 2005)
66 or lithospheric thinning (Cowie et al., 2005; Brune et al., 2014), or when border faults
67 become mechanically unfavourable for continued slip (Scholz and Contreras, 1998;
68 Goldsworthy and Jackson, 2001).

69 The overall mode of a rift (e.g. narrow vs wide *sensu* Buck, 1991 and Brun, 1999) is thought
70 to be predominately controlled by the interplay between Moho temperature, lithospheric
71 strength, crustal thickness, and strain rate (Buck, 1991; Brun, 1999; Huismans and
72 Beaumont, 2007). In contrast, the surface expression of a rift - whether faults form
73 symmetric grabens or asymmetric half-grabens, and the length, orientation and
74 segmentation of major faults - is controlled by crustal rheology (Huismans and Beaumont,
75 2007; Hodge et al., 2018). Within the East African Rift system, there is evidence for both
76 narrow and wide rift modes (*sensu* Buck, 1991; Ebinger and Scholz, 2012), symmetric and
77 asymmetric grabens (Ebinger et al, 1999; Lao Davila et al, 2015) and a range of relationships
78 between fault strike, metamorphic foliation, and regional stresses (Ring, 1994; Wheeler and
79 Karson, 1994; Dawson et al., 2018; Hodge et al., 2018; Williams et al., 2019). The lack of
80 constraints on strain distribution, geochronology and geophysical properties in East Africa
81 makes it challenging to ascertain the relative roles of shallow crustal rheology, heatflow,
82 crustal thickness and finite strain in shaping the geometry of incipient rift basins.

83 To investigate the geometry and strain distribution within a youthful rift, we analyse the
84 geomorphic signature of an active normal fault array in the Zomba Graben, which is at the
85 southern end of the incipient, amagmatic Malawi Rift. Although the topography across the
86 graben is dominated by a west-dipping border fault, we detect five previously unrecognised

active fault scarps using field data and geomorphic analysis of high-resolution topographic data. Our analysis suggests that current rift-related deformation is distributed on both the border faults and faults within the rift interior. Our findings have implications for our understanding of the evolution of strain in the early stages of continental rifting and the associated seismic hazard.

2. Tectonic and Geological Setting

2.1. The Malawi Rift

The ~ 900 km long Malawi Rift System is located at the southern end of the largely amagmatic western branch of the East African Rift System (EARS; Ebinger et al., 1987; Figure 1). The rift along Lake Malawi is defined by a series of asymmetric half-grabens with segmented border faults that offset Proterozoic medium to high grade metamorphic rocks with fabrics formed in multiple Precambrian orogenic events (Fritz et al., 2013). The border faults related to the current rift regime are up to ~120 km long, have throws of at least ~7-8 km and the hanging wall sediment thickness is at least 5 km (Contreras et al., 2000; Accardo et al., 2018; Shillington et al., 2020; Figure 1c-e). Sediment sequences observed in the hanging walls of these border faults decrease in thickness from >5 km in the north of the lake to ~1 km in the south (Scholz and Rosendahl, 1988; Specht and Rosendahl, 1989; Shillington et al., 2020). Faults have been mapped in Lake Malawi by a number of seismic reflection surveys carried out in the lake (Scholz and Rosendahl, 1988; Scholz, 1995; Mortimer et al., 2007; Lyons et al., 2011; Shillington et al., 2016) as well as a recent network of lake bottom and onshore seismometers in northern Malawi and Tanzania (Shillington et al., 2016; Accardo et al., 2018). These seismic surveys, along with the 2009 Karonga earthquake sequence that occurred within the hanging wall of the rift-bounding Livingstone

fault, indicate that both rift border and intrabasin faults are currently active at the northern end of the Malawi Rift (Biggs et al 2010, McCartney and Scholz 2016, Gaherty et al 2019). Active faulting is also occurring at the southern end of the lake, as demonstrated by the M_w 6.1 1989 Salima Earthquake (Jackson and Blenkinsop 1993).

Rifting within the western branch of the EARS is thought to have initiated in the Oligocene (~25 Ma; Roberts et al., 2012). Low temperature apatite thermochronology from samples in the northern basin of Lake Malawi indicates that rifting commenced at ~23 Ma (Mortimer et al., 2016). This is earlier than previously proposed age of ~9 Ma based on radiometric dating of volcanic and volcanoclastic deposits from northern Malawi (Ebinger et al., 1993). The age of the rift in central and southern Malawi is poorly-constrained. A 4.6 Ma age has been proposed for the onset of sediment accumulation in Lake Malawi's central basin (~350 km to the north of the Zomba Graben), from extrapolating the average rates of sediment accumulation in ~1.3 Ma drill core (Lyons et al 2015) to the entire sedimentary sequence (McCartney and Scholz 2016). This would suggest a gradual southward propagation of the rift (Ebinger et al., 1987; Contreras et al., 2000), which is consistent with sediment thickness and footwall topography decreasing from north to south along the rift (Specht and Rosendahl, 1989; Flannery and Rosendahl, 1990; Lao Davila et al., 2015). An alternative hypothesis is that the onset of extension is uniform along the Malawi Rift, but the extension rate is faster in the northern part of the rift because the Euler pole of the plates is located south of the Malawi Rift (Calais et al., 2006; Saria et al., 2014; Stamps et al., 2018). Although there are currently few constraints on the age of the EARS to the south of Lake Malawi (Dulanya, 2017), we consider it unlikely that extension initiated in this region prior to the onset of sedimentation in Lake Malawi. This places a poorly constrained approximate

maximum age of the rifting in the Zomba Graben as the mid-Miocene to early-Pliocene (Delvaux, 1995).

The onshore rift south of Lake Malawi consists of three linked half-grabens (Figure 1, Williams et al., 2019). The border faults have escarpment heights of <1000 m, and so are less prominent than those within the lake (Lao-Davila et al., 2015; Figure 1c-e). The Shire River, which has been the outlet of Lake Malawi since ~800 ka, flows through the centre of these grabens (Ivory et al., 2016; Figure 1). The NW-SE trending Makanjira Graben contains two known active intrabasin faults: the ~55 km long Malombe fault, and the ~110 km long Bilila-Mtakataka fault, a possible source of the 1989 M_w6.1 Salima earthquake (Jackson and Blenkinsop, 1993; Hodge et al., 2018; 2019). The graben is bounded by the Chirobwe-Ncheu and Mwanjage faults, although it is not known whether these are currently active or not. Immediately south of the Makanjira Graben lies the Zomba Graben, which is the focus of this study and described in more detail in section 2.2. To the south of the Zomba Graben, in the middle Shire Valley, the river drops by ~ 380 m in elevation with no evidence of active faulting (Dulanya, 2017; Figure 1). The NW-SE trending Lower Shire Graben lies ~60 km further south and is a reactivated Karoo-age basin bounded to the east by the 85 km long active Thyolo fault (Figure 1b; Hodge et al., 2019). The EARS continues south into the Urema Graben, the site of repeated seismic activity following the 2007 M_w7.0 Machaze earthquake (Lloyd et al, 2019; Copley et al., 2012).

Kinematic models of earthquake slip vectors and GPS measurements in the Malawi rift indicate an extension direction of 086° ± 5° (Saria et al., 2014; Stamps et al., 2018). The variation in the strike of the faults within the southern Malawi rift varies between NW-SE and NE-SW trending grabens. Consequently, many of the faults that have reactivated within

156 the rift are slightly oblique to the regional extension direction (Figure 1b; Williams et al.,
157 2019). Despite this, the available earthquake focal mechanisms and fault slickensides
158 indicate that the faults in the rift are reactivating as dip slip structures in the current rifting
159 regime (Williams et al., 2019).

160 *2.2. The Zomba Graben*

161 The Zomba Graben is a NE-SW trending segment of the onshore Malawi Rift where the
162 dominant structure is the NW-dipping Zomba fault. The Zomba Graben has traditionally
163 been considered a half-graben similar to those in Lake Malawi (e.g. Ebinger et al., 1987), but
164 Lao Davila et al. (2015) map it as a ~50 km wide full-graben, bounded to the west by the SE-
165 dipping Lisungwe fault (Figure 1e). Other than the disputed mapping of the rift border faults
166 at the edges of the graben, little is known about the pattern of faulting in this region or the
167 distribution of strain (Figure 1). A set of escarpments in the centre of the graben that offset
168 fluvio-lacustrine sediments have been variously mapped as 'terrace features' (Bloomfield,
169 1965; Figure 2), active fault scarps (Dixey, 1926) and inactive late-Jurassic or early
170 Cretaceous faults (Dixey, 1938).

171 The topography of the Zomba Graben is influenced by the structure and composition of the
172 basement complex, which comprises Proterozoic metamorphic rocks of the Southern
173 Irumide Belt and subsequent intrusions (Figure 2; Manda et al 2019). At the regional scale,
174 the rift follows the strike of the Southern Irumide foliation (Figure 1f). On the western side
175 of the rift, the Kirk Range is composed of metasedimentary schists, paragneisses and
176 granulites, and contrasts with the lower elevation eastern side, which is composed of meta-
177 igneous charnockitic granulites (Figure 2; Bloomfield and Garson, 1965). Syn- and post-
178 kinematic intrusions form local regions of high topography. The most notable of these are

the Proterozoic Chingale Ring Complex, and the Upper Jurassic-Lower Cretaceous Chilwa Alkaline Province, which formed during a phase of NE-SW extension (i.e. orthogonal to the current extension direction; Bloomfield 1965, Eby et al 1995; Castaing, 1991). Although the Zomba Massif, a quartz-syenite and granite intrusion, dates from this period, there is no evidence for contemporaneous Cretaceous-Jurassic age faults or sediments.

3. Active faults within the Zomba Graben

Active faults in Malawi are typically identified by the surface exposure of a continuous, steep scarp at the base of a footwall escarpment (Jackson and Blenkinsop, 1997; Hodge et al., 2018; 2019). Supplementary evidence is provided by observations of soft, unconsolidated hanging wall sediments, preserved uplifted river terraces in the footwall, and knickpoints in streams within <100 m of the fault scarps (Jackson and Blenkinsop, 1997). These criteria have been used prior to this study to identify three active faults south of Lake Malawi but outside the Zomba Graben: the Bilila-Mtakataka, Malombe and Thyolo faults (Figure 1c; Hodge et al., 2019). As no active faults had previously been documented in the Zomba Graben, geological maps were used to first identify faults where Bloomfield (1965) mapped Tertiary-Recent hanging wall sediments (Figure 3a). The detailed topographic analysis described below was then used to determine whether a fault has formed an active fault scarp, in which case it would be considered currently active. These satellite-based observations were used to target a 6-week field campaign in 2018, which confirmed the results and enabled more detailed analysis of the scarp morphology in a few selected locations.

3.1. Topographic analysis to assess fault activity

We used a TanDEM-X digital elevation model (DEM) of the Zomba Graben to identify and analyse fault scarps and the river channels that cross them (Figure 3). TanDEM-X DEMs have a horizontal resolution of 12.5 m and an absolute vertical mean error of ± 0.2 m (RMSE < 1.4 m; Wessel et al., 2018), which is sufficient for measuring the meter-scale fault scarps in the Zomba Graben (see Hodge et al., 2019 for discussion of DEM morphology and scarp height in this region). We considered the presence of a linear scarp coinciding with changes in channel incision and width, and hanging wall sediment deposition, as evidence for active faulting during the current rifting episode (Figure 3).

We produced slope maps from the DEM by calculating the scalar magnitude of the slope derivative using the grdgradient tool in the Generic Mapping Tools routines (Wessel and Smith, 1998; Figure 3b) and use these maps to identify the location of the active fault scarps. We noted any gaps in the scarps, or peaks and troughs in the displacement profiles, that may be indicative of fault segmentation (following Hodge et al., 2018). We extracted 500 m long fault-perpendicular topographic profiles every 12 m, and stacked them at 100 m intervals. The stacking has the effect of removing short-wavelength topographic features not related to the fault such as local sedimentation and erosion or human settlements and vegetation close to the fault. The scarp height was measured by fitting regression lines to the footwall and hanging wall topography of the stacked profiles, and calculating the vertical difference between the extrapolated regression lines at the point of maximum steepness on the scarp (Avouac, 1993; Figure 4a). To estimate the uncertainty, we applied a Monte Carlo approach by selecting 10,000 random subsets of points from the footwall and hanging wall, and allowing the exact location of the fault to vary. The variation between

223 profiles is due to a combination of differential geomorphic degradation of the fault scarp
224 and variation in fault offset that forms during an earthquake. Example profiles for each fault
225 are shown in Figure 4. We filter the resulting measurements along strike using a 3 km wide
226 moving median (Hodge et al., 2018; 2019).

227 Rivers that cross normal faults record information about the timing and magnitude of active
228 faulting in their long profile (Boulton and Whittaker, 2009). River long profiles, which plot
229 the change in elevation of the river channel with distance along the course of the river, can
230 therefore be used as an indicator of fault activity in regions where the location of active
231 faults is poorly constrained (Boulton and Whittaker 2009). For example, on rivers that cross
232 active normal faults, a change in uplift rate in the footwall of the fault leads to the river
233 channel responding transiently by becoming steeper and more incised upstream of the fault
234 (Whittaker et al., 2008). The knickpoints or knickzones that form as a result of this process
235 propagate upstream through time, with their vertical rate of propagation a function of the
236 magnitude of uplift rate change (Attal et al., 2008; 2011; Whittaker et al., 2008). We
237 extracted long profiles of rivers in the Zomba Graben with a drainage area greater than
238 6,000 m^2 using TopoToolbox (Schwanghart and Scherler, 2014). We identified changes in
239 channel steepness that are evidence of perturbations to the power-law relationship, $S = k_{sn}$
240 $A^{-\theta_{ref}}$, between local channel gradient, S, and upstream drainage area, A, in detachment
241 limited rivers (Whipple and Tucker 1999). We used a reference concavity index, $\theta_{ref} = 0.45$ to
242 calculate a normalised channel steepness index value, k_{sn}, using the 12.5 m resolution DEM,
243 thus facilitating a comparison between streams with a large range of drainage areas (Wobus
244 et al., 2006). Relatively high k_{sn} values reflect knickpoints or knickzones where river channels
245 are transiently adjusting to perturbations to the channel gradient-drainage area

relationship. Thus, we look for areas where linearly aligned increases in k_{sn} values coincide with our other morphological indicators of active faulting (Figure 3). Consistent along-strike increases in k_{sn} upstream of a fault, suggest a perturbation of the stream power law caused by changes in uplift rates by active normal faulting (Wobus et al., 2006; Figure 3d). In these cases, relatively lower k_{sn} values further upstream reflect the channel conditions prior to tectonic disturbance.

3.2. Description of fault scarps

Based on the topographic analysis we found evidence for five active fault scarps within the Zomba Graben that we subsequently confirmed during a 6-week field campaign in 2018. In this section, we describe the tectonic geomorphology and field observations of two border faults, Zomba and Lisungwe, and three intra-rift faults, Chingale Step, Mlungusi and Mtsimukwe. For each fault, we report the dimensions of the fault scarps discovered at the base of footwall escarpments (all measurements are listed in Tables S1-S6), and describe the other features that led us to conclude they are active. Examples of the fault scarps measured on each fault are shown in Figure 4. The measurements are shown in Figure 5 and summarised in Table 1.

The NW-dipping Zomba fault borders the eastern side of the Zomba Graben and has a ~50 km long escarpment with an active fault scarp at the base (Figure 5a & 5b and Figure S2). The mean height of the fault scarp is 15.6 ± 5.2 m (Figures 4a & 5b). The scarp height measurements show evidence for five 4-18 km long segments. Segment three has an asymmetric scarp height profile, with the highest scarp height measured at the northern end of the segment. The maximum scarp height in each segment varies between ~17 m and ~31 m, with the highest scarp height observed in the southernmost segment. Normalised

channel steepness values (K_{sn}) increase where rivers cross the fault (Figure S2d). Higher K_{sn} values 3-4 km into the hanging wall at the northern end of the fault are associated with the distal edges of alluvial fans (Figure S2d). The scarp is noticeably steeper adjacent to the Zomba Plateau and a ~2 km step to the northwest occurs between segments one and two, at the northern end of the fault in front of the Zomba Plateau (Figure S2b-c). At the northern end of the fault, triangular facets were observed in the field (Figure 6a). Large alluvial fans in the hanging wall are composed of material derived from the Zomba Plateau and appear to have been offset by the fault (Figure 6b). In the middle of the fault, a ~17 m high fault scarp (Figure 6c) contains a zone of highly fractured charnockite at its base (Figure 6d).

The NW-dipping Chingale Step fault (Figures 4a, 5a & 5c, and Figure S3) is located approximately 10 km into the hanging wall of the Zomba fault and has formed a ~40 km long scarp. The fault scarp shows evidence of multiple ruptures, with two scarps identified at numerous sites along the fault (Figure 4a). The lower scarp is steepest and is separated from the upper gentler dipping scarp by a break in slope (see also Figure S3). The steeper lower scarp suggests this rupture is younger than the upper scarp. We measured the height of both the lower scarp and the total height of the multiple scarp. The average height of the total scarp was 19.6 ± 12.1 m, comprised of three segments (Figure 5c). Segment lengths vary between 10 and 18 km, with a maximum total scarp height of 35.3 ± 14.6 m on the northern segment. In contrast, the lower scarp is not segmented, and the scarp height is approximately constant along the entire length of the fault (mean height of 5.7 ± 2.5 m; red line in Figure 5c).

Where river channels cross the Chingale Step fault, K_{sn} increases (Figure S3) and the upstream long profiles are oversteepened (Figure 7c-d and Figure S4). The elevation of the top of the oversteepened reaches, or knickpoints, changes along the strike of the fault (Figure 7a). The vertical difference between the fault and the top of the oversteepened reaches shows two segments, separated by a zone of linkage, which follow the shape of the fault scarp displacement profile (Figure 7). The boundaries between segments observed in the knickpoint elevations also corresponds to one of the segment boundaries identified in the scarp height profile. As the vertical movement of a knickpoint is controlled by the magnitude of the perturbation experienced by a river channel (Attal et al., 2008; 2011; Whittaker et al., 2008) the correspondence between the knickpoint elevations and the along strike scarp height suggests that a change in fault uplift rate is controlling a transient channel response (Figure 7). Furthermore, the river channel within the linkage zone shows two knickpoints, which is likely related to the separate initiation of faulting of the southern and northern segments (Figure 7c). The consistent offset measured across the lowermost fault scarp (red line in Figure 5c) suggests that these segments have linked in the time since the active fault scarp begun to be preserved, and are now operating as a single fault. A scarp was visible along all sections visited, with a zone of fault gouge and fractured basement rocks at the base of the fault scarps in exposed stream beds (Figure 8). At the Kalira river site, the fault surface itself was visible with a polished surface and slickensides (Figure 8). The multiple scarp was not visible in the field, although most accessible locations were on the southern end of fault where the difference between the total scarp and the lowermost scarp was smaller than along the northern segment of the fault.

313 The SE-dipping Mlungusi fault has formed a ~20 km long scarp in the centre of the Zomba
314 Graben (Figures 4a, 5a & 5d) and has a mean scarp height of 6.9 ± 3.1 m. The slope map
315 shows a prominent scarp along the entire length of the fault (Figure S5), except in two
316 locations where rivers flow along the fault (Figure 5d). In contrast, K_{sn} values are only
317 elevated in the centre of the fault (Figure S5d). The Shire River crosses from the hanging
318 wall into the footwall at the southern end of the Mlungusi fault, where it changes from a
319 wide, meandering channel with a floodplain in the hanging wall, to a narrow, incised
320 channel with an associated set of rapids as it crosses into the footwall (Figure 9). Along
321 strike from this location, a steep fault scarp was observed in the field (Figure 9c) which has
322 offset fine-grained fluvial-lacustrine deposits found on the floor of the graben. The fault
323 scarp height profile (Figure 5d) possibly shows evidence of a segment boundary in the
324 centre of the fault, although obvious segmentation is obscured by erosion of the fault scarp
325 by the Shire River (Figure 5d). In the centre of the fault the scarp is covered by clast-
326 supported rounded to subrounded pebbles within a sandy matrix, which we interpret as
327 lacustrine beach deposits (Figure 9c). Long-term footwall uplift has led to drainage
328 reorganisation as rivers draining into the axial Mtsimukwe River in the footwall of the
329 Mlungusi fault are restricted to the western side of the channel, distal to the fault (Figure
330 S5d).

331 The E-dipping Mtsimukwe fault has formed a ~13 km long scarp trending ~N-S (Figures 4a,
332 5a & 5e). The mean scarp height is 3.6 ± 0.7 m. The slope map shows that the fault scarp is
333 best preserved in the central part of the fault except a ~2 km long section where the fault
334 intersects a road (Figure S6b). The streams that cross the fault show a small increase in K_{sn}

335 value, with the largest increase in centre of the fault, but there is no evidence of
336 segmentation (Figure S6).

337 The E-dipping Lisungwe fault is the western border fault of the Zomba Graben (Figure 2, 5a
338 & 5f). High slope values have a linear trend aligned with an increase in K_{sn} in the streams
339 that cross the escarpment (Figure S7). The mean offset across the fault scarp is 10.0 ± 6.7 m
340 (Figures 4a & 5f). No fieldwork was conducted on the Mtsimukwe and Lisungwe faults due
341 to access reasons, but the remote sensing observations described above and seen in Figure
342 S6 and Figure S7 are similar to the observations on faults (e.g. Zomba, Chingale Step and
343 Mlungusi faults) where fieldwork was able to confirm the evidence gained remotely.

344 *3.3. Fault Kinematics and Extension Direction*

345 Slickensides along the Chingale Step fault (Figure 8b-d; plunging 52° towards 301°) and
346 kinematic indicators on faults elsewhere in the Zomba Graben (Bloomfield, 1965; Chorowicz
347 and Sorlien, 1992) indicate an approximately NW-SE extension direction (Williams et al.,
348 2019). This extension is orthogonal to the surface traces (015 ± 11°) of the five faults,
349 indicating a generally dip-slip displacement (Williams et al., 2019). This contradicts previous
350 rift-wide estimates of extension (Delvaux and Barth, 2010; Figure 1). However, these
351 estimates likely reflect that normal faulting events in the Malawi Rift are approximately
352 purely dip-slip despite regional changes in fault strike (Williams et al., 2019), as also
353 indicated by the 2009 Karonga Earthquakes (Biggs et al., 2010), the 1989 Salima earthquake
354 (Jackson and Blenkinsop, 1993), and a M_w=5.6 earthquake in March 2018 (red focal
355 mechanism in Figure 1b). An extension azimuth of 072° is recorded geodetically at Zomba
356 (Figure 1; Stamps et al., 2018) in contrast to the NW-SE extension in the Zomba Graben. This
357 variation in extension direction is consistent with previous observations of deviation

between local and regional extension directions in Malawi (Delvaux and Barth, 2010; Hodge et al., 2018; Williams et al., 2019).

3.4 Age of the fault scarps

The faults in the Zomba Graben have offset the sedimentary cover on the floor of the graben, which includes coarse-grained sandstones of the Matope beds, as well as sandy, pebbly, fluvio-lacustrine deposits in the centre of the rift (Figure 2). Both of these sediment packages were likely deposited in the Late Quaternary (since ~800 ka) reflecting fluctuations in the level of Lake Malawi. Prior to the Mid-Pleistocene Transition (MPT; ~800 ka), Lake Malawi was much shallower than the present day and likely drained through an outlet at the northern end of the lake (Ivory et al., 2016). Since the MPT, Lake Malawi experienced a significant base level rise, and now fluctuates between high-stand and low-stand conditions (up to ~500 m lower) and now outlets through the Shire River valley into the Zambezi River (Ivory et al., 2016; Lyons et al., 2015; McCartney and Scholz, 2016; Owen et al, 1990). Since ~75 ka, high-stand conditions have prevailed, during which lake levels may have been up to ~150 m higher than present (Lyons et al., 2015; McCartney and Scholz, 2016). The floor of the Zomba Graben lies ~10 m above the current lake level, therefore during high-stands, lacustrine sediments will have been deposited in the graben, whereas low-stands were accompanied by the deposition of coarse-grained sediments (Lyons et al., 2011; 2015).

We conclude that the observed fault scarps have formed during the Late Quaternary time period: <800 ka and maybe as recently as <75 ka as they offset and have been draped by both fine and coarse-grained sediments. A number of observations are consistent with this interpretation: i) The fault scarps are generally steep (Figure 3b & Figure 4a); ii) Scarp diffusion modelling on the Bilila-Mtakataka fault, to the north of the Zomba Graben, suggests a ~20 m high fault scarp formed within the last 6.4 ± 4 ka (Hodge et al., 2020).

Although this age represents the age of the scarp, not the fault itself, and is heavily dependent on the diffusion age used in the modelling, which is poorly constrained, it nonetheless demonstrates that the fault scarps observed in southern Malawi are active in the Late Quaternary. iii) the Mlungusi fault is draped by a layer of clast-supported, sub-rounded to rounded cobbles in a sandy matrix, consistent with a lacustrine palaeobeach deposit, which was likely deposited during a Late Quaternary high-stand within Lake Malawi (since the MPT ~800 ka); and iv) Optically-Stimulated Luminescence (OSL) ages for surficial palaeo-fluvio-lacustrine deposits near Lake Chilwa, 20-30 km to the east of the Zomba Graben, are <50 ka (Thomas et al., 2009; Figure 1).

The measured scarp heights (Section 3.2) are generally greater than empirically derived single event displacement values for normal faults (e.g. Leonard, 2010). Therefore, and based on the relative age constraints above, the scarps should be viewed as composite scarps representing the cumulative offset from multiple earthquakes during the Late Quaternary (see Hodge et al., 2020 for a discussion on this).

4. Strain distribution across the Zomba Graben

We found evidence for five Late Quaternary active faults within the Zomba Graben. The across strike spacing between the active faults is approximately 10-15 km and the maximum height of each fault scarp ranges between 9.5 ± 4.2 m and 35.3 ± 14.6 m (Figure 5). The distribution of fault scarps within the graben is a notable feature. The highest fault scarp was found along the Chingale Step fault (Figure 5c), which is located in the hanging wall of the border fault (Figure 5a). Thus, the strain within the Zomba Graben over the time period that the active fault scarps have formed is not localised on a single major border fault but instead distributed across the width of the rift (Figure 5a).

We estimate the cumulative strain since the formation of the fault scarps, assuming an approximately uniform age of the fault scarps. We calculate finite strain across the Zomba Graben using the England and Molnar (1997) adaptation of the Kostrov (1974) expression of strain rate:

$$\bar{\varepsilon}_{ij} = \frac{1}{2a}\sum_{k=1}^{k}\frac{L^k \bar{s}^k}{\sin\vartheta^k}\left(\hat{u}_i^k \hat{n}_j^k + \hat{u}_j^k \hat{n}_i^k\right) \qquad (1)$$

where a is the surface area of the region, L^k is the length of fault k in that region, s^k is the slip of fault k in that region, ϑ^k is the dip of fault k, $\hat{u}^k$ is a unit vector of fault k in the direction of slip and $\hat{n}^k$ is a unit vector of fault k normal to the fault plane. The advantage of this adaption is that it is independent of seismogenic thickness or shear modulus. We assume pure dip-slip faults that strike parallel to each other (see section 3.3), such that ε_{22} is equal to zero, and ε_{11} is perpendicular to the mean strike of the faults. The only unknown term is fault dip, for which we assume an Andersonian value of 60°, although using a randomly selected fault dip, within the usual range for normal faults (45°-60°; Collettini and Sibson 2001), produces similar results (Figure S8). We calculated the strain within 5 km (across strike) by 50 km (along strike) rectangular boxes with long axes orientated 200°, using the maximum scarp height measured along each fault as a proxy for fault throw (following Hodge et al., 2018).

The strain associated with the fault scarps has dominantly occurred across the Chingale Step fault (42 ± 17 %) and the Zomba border fault (40 ± 17%), both west-dipping faults on the eastern side of the graben (Figure 10c). The proportion of strain across both east-dipping intrabasin faults (Mtsimukwe: 6 ± 6 % and Mlungusi: 7 ± 1 %) and the east-dipping border fault (Lisungwe: 6 ± 3 %; Figure 10c) are all the same within error. The proportion of strain

accommodated across the east-dipping intrabasin faults (13 ± 6%) is within the error of the proportion of strain accommodated on the border fault (6 ± 3 %). On the west dipping faults, there is no significant difference between strain on the intrabasin (42 ± 17 %) and border faults (40 ± 17%). Across the whole graben, the proportion of strain that has occurred across the intrabasin faults (55 ± 24 %) and the proportion of strain across the border faults (45 ± 20 %) is roughly equal, although we note the large error bars. This equates to 18.1 ± 7.1 m of finite extension on the intrabasin faults and 14.9 ± 6.7 m of finite extension on the border faults (Figure 10c). The east dipping faults have accommodated 6.1 ± 3.1 m of finite extension whereas the west dipping faults have accommodated 26.9 ± 11.4 m.

5. Discussion

5.1 Strain Migration and Fault Evolution during rifting

Current conceptual models suggest that following an initial stage of distributed deformation, the transition from rift border faults to intra-rift deformation occurs over timescales of 10-15 Ma in the East African Rift as lithospheric thinning leads to asthenospheric upwelling and production of magmatic fluids (Ebinger, 2005; Ebinger and Scholz, 2012; Buck, 2004; Huismans and Beaumont, 2014). Here we compare our observations from the early-stage Zomba Graben with those from elsewhere in the East African Rift and discuss the implications for the evolution of strain distribution during rift development.

In the Zomba Graben, we observe that 55 ± 24% of the strain is accommodated on intra-rift faults (Figure 10). While this level of intra-rift strain is commonly observed in magmatic rift segments (e.g. Bilham et al., 1999; Ebinger and Casey, 2001), this is far higher than other

amagmatic rifts. In the ~10 Ma, magma-poor Lake Tanganyika Rift, the border faults accommodate 90% of extensional strain (Muirhead et al., 2019). Within the northern basin of Lake Malawi, Mortimer et al. (2007) inferred that activity on intra-rift faults diminished over the lifetime of the rift. In contrast, seismic reflection profiles from the central basin of Lake Malawi show that intra-rift faults have been active over the lifetime of the amagmatic rift (McCartney and Scholz, 2016), but these same profiles were unable to constrain the activity on border faults over the same time period.

There are two possible explanations for the roughly equal distribution of deformation between the intra-rift faults and the rift border faults that we observe in the Zomba Graben (Figure 10): 1) the current distribution represents a period of time prior to the localisation of strain across the rift border faults; or 2) deformation has migrated from the border faults onto intra-rift structures. Topographic profiles across the northern and central basins of Lake Malawi show that the largest topographic expression is associated with the major border fault(s) at the edge of the rift (Figures 1c & 1d). Within the Zomba Graben, although the border faults are less developed, they still have the largest topographic expression (Figure 1e). This suggests that that over the lifetime of the rift, the Zomba fault, and possibly the Lisungwe fault, have experienced more cumulative displacement than the intra-rift faults (Figure 1e). Thus, we prefer an interpretation where the approximately even distribution of active strain between border and intra-rift faults has developed after a phase of heightened border fault activity but before observable magmatism. We discuss four mechanisms that may explain this pattern of strain across a distributed network of faults in an apparently non-volcanic rift: 1) cessation of border fault activity; 2) lithospheric flexure; 3) a cryptic fluid phase; and 4) transient changes associated with fault network evolution

and fault linkage. We then discuss whether the pattern of strain can be explained by the lithospheric structure, including crustal heterogeneities.

5.1.1 Cessation of Border Fault Activity and Lithospheric Flexure

The maximum amount of displacement a normal fault can accumulate, before it becomes more favourable to form a new fault, is thought to be controlled by a combination of effective elastic thickness, seismogenic thickness, and surface processes, such as footwall erosion and hanging wall deposition (Scholz and Contreras, 1998; Olive et al., 2014). The exact mechanism of fault abandonment is debated but it generally requires large total displacements (>5 km) that lead to an increase in the flexural restoring force and/or rotation of the fault dip to unfavourable angles (Scholz and Contreras, 1998; Goldsworthy and Jackson, 2001).

When rift border faults are abandoned, migration of fault activity into the hanging wall of the previously active fault is widely observed (see Goldsworthy and Jackson, 2001, for further discussion). Accardo et al. (2018) propose that the >7 km of throw on the border faults in the northern and central basins of Lake Malawi indicates that these faults are approaching their maximum size and that the migration of strain into the rift interior is imminent or now occurring (e.g. the Karonga earthquake sequence; Biggs et al., 2010; Kolawole et al., 2018). However, this mechanism is unlikely to cause the intra-rift faulting in the Zomba Graben, because both the border and intra-rift faults have been active during the Late Quaternary and the topographic relief is relatively small (<1 km). Similarly, bending forces associated with flexure of the border fault hanging wall can induce strain in the intra-rift region within the upper crust, and although this has been proposed for Lake Malawi (Kolawole et al., 2018), the low throws and thick elastic crust (~30 km) in the Zomba Graben

would generate negligible flexural strain (Jackson and Blenkinsop 1997, Muirhead et al 2016).

5.1.2 Influence of fluids

Magma-assisted rifting, where magmatic fluids and volatiles enable extension at lower stresses than the available tectonic forces, is thought to play an important role in facilitating rifting in thick continental lithosphere (Buck, 2004; Ebinger et al., 2017). There is no evidence of active magmatic activity or more than a few kilometres of crustal thinning in the Zomba Graben (Reed et al., 2016, Wang et al., 2019). Furthermore, the geochemistry of hot springs in southern Malawi does not suggest a magmatic influence (Dulanya et al., 2010) and the nearest active volcano, Rungwe, is located ~700 km to the north (Figure 1). However, decompression melting or lower crustal magmatic intrusion might not lead to perceptible surface effects, and there is evidence for non-zero crustal thinning beneath southern Malawi (Wang et al., 2019). In an example further south and west in the EARS, low seismic velocities suggest decompression melting in the upper asthenosphere of the Okavango Delta, despite a very low level of extension and no surface volcanism or evidence for mantle upwelling (Yu et al., 2017).

Earthquakes occur in Malawi throughout the 38-42 km thick crust (Tedla et al., 2011; Jackson and Blenkinsop, 1993; Craig et al., 2011), consistent with estimates of effective elastic thickness in excess of 30 km (Ebinger et al., 1999). This can occur in magmatic rift zones if border faults penetrate into the lower crust, or if melt and volatile migration into the lower crust causes localised weakening, which can also trigger seismicity (Ebinger et al., 2017). However, in northern Malawi, there is little difference between the focal depth of earthquakes on the intrabasin and border faults (Ebinger et al., 2019). Current imaging of the lower crust in Malawi does not allow us to discriminate between these mechanisms and

alternative explanations for the deep seismicity include 1) a dry, strong, granulite facies lower crust (Jackson et al., 2004), 2) above average lithospheric thickness (Chen and Molnar, 1983), or 3) localised zones of weak rheology within a strong, elastic lower crust (Fagereng, 2013).

5.1.3 Transient Changes Associated with Fault Evolution

The process of fault segment linkage can lead to an increase in fault slip rates over timescales of ~100 ka (Taylor et al., 2004). This can subsequently enable a newly linked fault to accommodate a greater proportion of the regional extension rate (Taylor et al., 2004; Cowie et al., 2005). The cumulative scarp on the Chingale Step fault is segmented but the steepest, most recent scarp on the fault cuts across the segment boundaries and is continuous and ~6 m high along the length of the fault (Figure 5b). As well as indicating that faults can rupture multiple segments simultaneously, it suggests that segment linkage has occurred. This implies that faults in this region grow through linkage that occurs before they have accumulated significant (i.e. >1 km) offsets and on short timescales of < 800 ka (and possibly <~50 ka). This rapid linkage, before continued slip accumulation, is consistent with the recent hybrid fault growth model where slip accumulates at a constant fault length after an initial growth phase (Rotevatn et al., 2019).

Observations from the Livingstone fault, northern Lake Malawi, suggest that permanent segment linkage that occurred during the past ~1.6 Ma has caused displacement rates to become greatest in the locations that were previously between segments (Mortimer et al., 2016). The segment linkage we observe along the Chingale Step fault is not associated with higher displacements at the previous segment boundary locations compared with locations along the rest of the fault (Figure 5b). When faults are closely spaced, as they are in the Zomba Graben, across-strike co-seismic elastic stress changes can drive transient variations

in slip rates on individual faults over the time scale of a few earthquake cycles (Cowie et al., 2012). With only one example, we cannot tell whether the displacement that has accumulated on the Chingale Step fault scarp across the segment boundaries is a long-lived feature of the rift, or a transient feature only representative of the time window we sampled (i.e. since the fault scarps have been preserved in the Late Quaternary). Nonetheless, although elastic fault interactions are likely contributing to the temporal evolution of strain across the network of faults in the Zomba Graben, they cannot explain the initial formation of a distributed fault network.

5.1.4 Lithospheric Structure

The roles of crustal thickness, lower crustal rheology, and lithospheric thermal structure in developing end-member narrow or wide rifts have been well studied (e.g. Buck, 1991; Huismans and Beaumont, 2007). Typically, strain in narrow rifts concentrates in the weakest part of the lithosphere while in wide rifts, lower crustal viscous flow drives distributed deformation in the upper crust (Buck, 1991). Southern Africa has unusually thick continental lithosphere (140-180 km; Craig et al., 2011) and crust (38-42 km thick; Tedla et al., 2011; Wang et al 2019), resulting from multiple episodes of orogenic thickening (Fritz et al., 2013). The available constraints on the lithospheric properties of the Zomba Graben suggest that conditions are similar to the very young (120-40 Ka) Okavango Rift (Craig et al., 2011). However, we have demonstrated that strain within the narrow (<50 km) Zomba Graben is distributed whereas the Okavango Rift is >150 km wide and deformation is localised to <50 km wide zones at the edges of the rift (Ebinger and Scholz, 2012). Thus, the currently-available constraints on lithospheric thickness and thermal structure cannot explain the differences between these two rifts.

In the Okavango rift, early localization onto a single border fault has been inferred to arise from deformation along a localised, pre-existing weakness (Kinabo et al., 2008). This early localisation differs from predictions by numerical simulations, which demonstrate that a strong, ductile lower crust promotes distributed faulting due to enhanced upper crustal fault interactions during rifting (Heimpel and Olson, 1996). The crust in southern Malawi is made up of high grade metamorphic rocks that lack hydrous minerals with low friction coefficients (Hellebrekers, et al., 2019), and exposed fault rocks are not demonstrably different in composition from these high grade basement rocks (Williams et al., 2019). At some local scales, for example along the Chingale Step fault, the faults cross-cut the foliation orientation. Thus, although the Zomba Graben follows the trend of the regional foliation, distributed faulting cannot be attributed to continued reactivation of pre-existing frictionally weak planes in the brittle regime. However, lateral heterogeneity in the lower crust, such as an anastomosing shear zone system, would enable strain localisation in lower viscosity zones in an otherwise cold, strong layer (Fagereng, 2013). Such localisation at depth may guide deformation patterns in the overlying brittle crust, such as the oblique strike of faults in southern Malawi, relative to the regional extension direction (Hodge et al., 2018; Williams et al., 2019).

The hypothesis of a lower crust with rheological heterogeneity: i) satisfies the requirements for a dominantly strong lower crust; ii) can, with sufficient velocity-weakening material (Hellebrekers et al., 2019), explain the deep seismicity observed in the Malawi rift; iii) facilitates the formation of a distributed fault network at the surface; iv) does not require pre-existing frictional weaknesses in the upper crust; and v) can explain the pure dip behaviour of the faults in an oblique rift (Philippon et al., 2015; Williams et al., 2019). This

suggests that patterns of strain distribution in amagmatic rifts may not be solely controlled by rift maturity; instead, scale, geometry, and degree of rheological heterogeneity in the lower crust, as well as elastic fault interactions in the upper crust may also be important.

5.3 Implications for Seismic Hazard.

Our analysis of high-resolution satellite topography has identified five active faults in the Zomba Graben, but current assessments of seismic hazard in Malawi do not extend south of Lake Malawi (Midzi et al., 1999; Hodge et al., 2015). Based on standard scaling laws (Leonard, 2010), these 15-50 km long faults could host earthquakes of Mw 6.3-7.1, assuming that faults do not fail in smaller individual segments, and that multiple separate faults do not slip in the same event. The administrative regions within 30 km of the Zomba Graben contains ~22% of the Malawian population (~ 4 million people), including the major population and administrative centres of Blantyre (population: ~800,000) and Zomba (population: ~100,000; Malawi National Statistics Office, 2018). The proximity of these newly-identified faults to this number of people presents a significant challenge for both seismic risk and regional development. Furthermore, the path of the Shire River is strongly affected by rift topography, and a large earthquake on the Mlungusi fault in particular could affect both irrigation and flooding on a regional scale as well as dam stability on the Shire River. This is particularly important as ~80% of Malawi's electricity is generated by hydroelectric dams within the middle Shire valley (Taulo et al., 2015).

In slowly deforming regions and/or regions with poor seismic detection infrastructure, instrumental catalogues are unlikely to record a representative enough sample of seismicity to sufficiently assess seismic hazard. Including fault maps in probabilistic seismic hazard analysis can overcome this problem (e.g. Hodge et al., 2015; Chartier et al., 2017; Pace et al.,

2018), but this requires estimates of both earthquake magnitude and recurrence interval. In Lake Malawi, where fault slip rates have not been measured, Hodge et al. (2015) assigned the plate motion to individual faults in their hazard assessment. However, the discovery of multiple, subparallel fault scarps in the Zomba Graben suggests longer earthquake recurrence times and lower probabilities of peak ground acceleration for a given return period. Furthermore, increases in the number of faults within a region also leads to more variable fault slip rates, which in turn can result in earthquake clusters (Cowie et al., 2012). The 2009 Karonga earthquake sequence in northern Malawi illustrates that such clusters occur in the East African Rift (Biggs et al., 2010), but instrumental records are not sufficient to determine how widespread this behaviour is. Earthquake clusters present an additional challenge for seismic hazard assessment as they are not captured by time-independent probabilistic seismic hazard assessments.

5 Conclusions

We use high-resolution TanDEM-X topography to find and measure active faults scarps in the Zomba Graben in southern Malawi. We show that the active fault scarps occur at the base of the rift border faults and also on the rift floor between them. The strain calculated from the heights of the fault scarps is roughly equally distributed between the rift border faults and the intrabasin faults. This presents new insights into the behaviour of rifts during the incipient stages of continental extension in a region of thick lithosphere and no active volcanism. In contrast to the prevailing paradigm, it suggests that during the early, amagmatic stages of continental rifting, a significant portion of the extension can occur on intra-rift faults.

Active intrabasin faults have previously been documented during early rifting (McCartney and Scholz, 2016), but they have been inferred to be subsidiary to the border faults (Muirhead et al., 2019). The strain distribution across the rift in the Zomba Graben show that early-rift intrabasin faults can accommodate a similar proportion of extension to the border faults. Therefore, while the overall mode of rifting is likely to be controlled by the rheology of the lithosphere, we suggest that upper-crustal fault interactions and strength variations within the lower crust can lead to spatially distributed and temporally transient faulting within early stage rifts. Finally, we find that the onshore rift in Southern Malawi represents a significant, but previously unappreciated source of seismic hazard within the East African Rift.

6 Acknowledgements

This work was funded by the EPSRC project 'Prepare' (EP/P028233/1), funded under the Global Challenges Research Fund. We thank Kondwani Dombola for his assistance with fieldwork planning and logistics. TanDEM-X data were obtained via DLR proposal DEM_GEOL0686. We thank Donna Shillington, an anonymous reviewer and the associate editor for reviews that improved this manuscript. Fault scarp profiles and scarp height data are available in the supplementary material and have also been archived within the Zenodo data repository at: http://doi.org/10.5281/zenodo.3582282

7 References

Accardo, N. J., Shillington, D. J., Gaherty, J. B., Scholz, C. A., Nyblade, A. A., Chindandali, P. R. N. et al. (2018). Constraints on Rift Basin Structure and Border Fault Growth in the Northern Malawi Rift From 3-D Seismic Refraction Imaging. *Journal of Geophysical Research: Solid Earth*. https://doi.org/10.1029/2018JB016504

658 Attal, M. Tucker, G. E., Whittaker, A. C., Cowie, P. A., & Roberts, G. P. (2008). Modeling
659 fluvial incision and transient landscape evolution: Influence of dynamic channel
660 adjustment. *Journal of Geophysical Research: Earth Surface*, 113, F3.
661 https://doi.org/10.1029/2007JF000893
662 Attal, M. Cowie, P. A., Whittaker, A. C., Hobley, D. Tucker, G. E., & Roberts, G. P. (2011).
663 Testing fluvial erosion models using the transient response of bedrock rivers to
664 tectonic forcing in the Apennines, Italy. *Journal of Geophysical Research: Earth*
665 *Surface*, 116, F2. https://doi.org/20.1029/2010JF001875
666 Avouac, J-P. (1993). Analysis of scarp profiles: Evaluation of errors in morphological dating.
667 *Journal of Geophysical Research: Solid Earth*, 98(B4), 6745-6754.
668 https://doi.org.10.1029/92JB01962
669 Biggs, J., Nissen, E., Craig, T., Jackson, J., & Robinson, D. P. (2010). Breaking up the hanging
670 wall of a rift-border fault: The 2009 Karonga earthquakes, Malawi. *Geophysical*
671 *Research Letters*, 37, L11305. https://doi.org/10.1029/2010GL043179
672 Bilham, R. Bendick, R. Larson, K. Mohr, P., Braun, J. Tesfaye, S. & Asfaw, L. (1999). Secular
673 and tidal strain across the Main Ethiopian Rift. *Geophysical Research Letters*, 26(18),
674 2789-2792. https://doi.org/10.1029/1998GL005315
675 Bloomfield, K. (1965). The Geology of the Zomba Area. *Bulletin of the Geological Survey*
676 *Department, Malawi*, 16, 223p.
677 Bloomfield, K., & Garson, M. S. (1965). The Geology of the Kirk Range-Lisungwe Valley Area.
678 *Bulletin of the Geological Survey Department, Malawi*, 17, 239p
679 Boulton, S. J., & Whittaker, A. C. (2009). Quantifying the slip rates, spatial distribution and
680 evolution of active normal faults from geomorphic analysis: Field examples from an

681 oblique-extensional graben, southern Turkey. *Geomorphology*, 104, 299-316.
682 https://doi.org/10.1016/j.geomorph.2008.09.007
683 Brun, J.-P. (1999). Narrow rifts versus wide rifts: inferences for the mechanics of rifting from
684 laboratory experiments. *Philosophical Transactions of the Royal Society A*,
685 357(1753). https://doi.org/10.1098/rsta.1999.0349
686 Brune, S. (2014). Evolution of stress and fault patterns in oblique rift systems: 3-D numerical
687 lithospheric-scale experiments from rift to breakup. *Geochemistry, Geophysics,*
688 *Geosystems*, 15(8), 3392-3415. https://doi.org/10.1002/2014GC005446
689 Brune, S. Heine, C. Pérez-Gussinyé, M. & Sobolev, S. V. (2014). Rift migration explains
690 continental margin asymmetry and crustal hyper-extension. *Nature communications*,
691 5. https://doi.org/10.1038/ncomms5014
692 Buck, W. R. (1991). Modes of continental lithospheric extension. *Journal of Geophysical*
693 *Research: Solid Earth*, 96(B12), 20161-20178. https://doi.org/10.0129/91JB01485
694 Buck, W. R. (2004). Consequences of asthenospheric variability on continental rifting. In G.
695 D. Karner, N. W. Driscoll, B. Taylor, D. L. Kohlstedt (Eds), *Rheology and Deformation*
696 *of the Lithosphere at Continental Margins* (pp. 1-30). New York: Columbia University
697 Press.
698 Calais, E., Ebinger, C., Hartnady, C., & Nocquet, J. M. (2006). Kinematics of the East African
699 Rift from GPS and earthquake slip vector data. *Geological Society, London, Special*
700 *Publications*, 259, 9-22. https://doi.org/10.1144/GSL.SP.2006.259.01.03
701 Castaing, C., 1991, Post-Pan-African tectonic evolution of South Malawi in relation to the
702 Karroo and recent East African rift systems: Tectonophysics, v. 191, p. 55–73,
703 doi:10.1016/0040-1951(91)90232-H.

704 Chartier, T. Scotti, O. Clément, C. Jomard, H. & Baize, S. (2017). Transposing an active fault
705 database into a fault-based seismic hazard assessment for nuclear facilities – Part 2:
706 Impact of fault parameter uncertainties on a site-specific PSHA exercise in the Upper
707 Rhine Graben, easter France. *Natural Hazards Earth System Science*, 17, 1585-1593.
708 https://doi.org/10.5194/nhess-17-1585-2017
709 Chen, W.-P., & Molnar, P. (1983). Focal depths of intracontinental and intraplate
710 earthquakes and their implications for the thermal and mechanical properties of the
711 lithosphere. *Journal of Geophysical Research: Solid Earth*, 88(B5), 4183-4214.
712 https://doi.org/10.1029/JB088iB05p04183
713 Chorowicz, J., & Sorlien, C. (1992). Oblique extensional tectonics in the Malawi Rift, Africa.
714 *GSA Bulletin*, 104(8), 1015-1023. https://doi.org/10.1130/0016-
715 7606(1992)104<1015:OETITM>2.3.CO;2
716 Collettini, C., Sibson, R. H. (2001). Normal faults, normal friction? *Geology*, 29(10), 927-930.
717 https://doi.org/10.1130/0091-7613(2001)029<0927:NFNF>2.0.CO;2
718 Contreras, J., Anders, M. H., & Scholz, C. H. (2000). Growth of a normal fault system:
719 observations from the Lake Malawi basin of the east African rift. *Journal of Structural*
720 *Geology*, 22(2), 159-168. https://doi.org/10.1016/S0191-8141(99)00157-1
721 Copley, A., Hollingsworth, J., & Bergman, E. (2012). Constraints on fault and lithosphere
722 rheology from the coseismic slip and postseismic afterslip of the 2006 Mw7.0
723 Mozambique earthquake. *Journal of Geophysical Research: Solid Earth*, 117, B03404.
724 https://doi.org/10.1029/2011JB008580
725 Corti, G. (2009). Continental rift evolution: From rift initiation to incipient break-up in the
726 Main Ethiopian Rift, East Africa. *Earth-Science Reviews*, 96(1-2) 1-53.
727 https://doi.org/10.1016/j.earscirev.2009.06.005

728 Cowie, P. A. (1998). A healing-reloading feedback control on the growth rate of seismogenic
729 faults. *Journal of Structural Geology*, 20(8), 1075-1087.
730 https://doi.org/10.1016/S0191-8141(98)00034-0
731 Cowie, P. A., Gupta, S., & Dawers, N H. (2000). Implications of fault array evolution for
732 synrift depocenter development: insights from a numerical fault growth model.
733 *Basin Research*, 12(3-4), 241-261. https://doi.org/20.1111/j.1365-
734 2117.2000.00126.xCowie, P. A., Underhill, J. R., Behn, M. D., Lin, J., & Gill, C. (2005).
735 Spatio-temporal evolution of strain accumulation derived from multi-scale
736 observations of Late Jurasic rifting in the northern North Sea: A critical test of
737 models of lithospheric extension. *Earth and Planetary Science Letters*, 234, 401-419.
738 https://doi.org/10.1016/j.epsl.2005.01.039
739 Cowie, P. A., Roberts, G. P., Bull, J. M. & Visini, F. (2012). Relationships between fault
740 geometry, slip rate variability and earthquake recurrence in extensional settings.
741 *Geophysical Journal International*, 189(1), 143-160. https://doi.org/10.1111/j.1365-
742 246X.2012.05378.x
743 Craig, T. J., Jackson, J. A., Priestley, K., & McKenzie, D. (2011). Earthquake distribution
744 patterns in Africa: their relationship to variations in lithospheric and geological
745 structure, and their rheological implications. *Geophysical Journal International*,
746 185(1), 403-434. https://doi.org/10.1111/j.1365-246X.2011.04950.x
747 Dawson, S. M., Laó-Dávila, D. A., Atekwana, E. A., & Abdelsalam, M. G. (2018). The influence
748 of the Precambrian Mughese Shear Zone structures on strain accommodation in the
749 northern Malawi Rift. *Tectonophysics*, 722, 53-68.
750 https://doi.org/10.1016/j.tecto.2017.10.010

751 Delvaux, D. (1995). Age of Lake Malawi (Nyasa) and water level fluctuations. *Musée Royal*
752 *Africque Centrale, Tervuren (Belgique), Department de Geologie et Mineralogies*
753 *Rapport Annuel,* 99-108.
754 Delvaux, D., & Barth, A. (2010). African stress pattern from formal inversion of focal
755 mechanism data. *Tectonophysics*, 482, 105-128.
756 https://doi.org/10.1016/j.tecto.2009.05.009
757 Dixey, F. (1926). The Nyasaland Section of the Great Rift Valley. *The Geographical Journal*,
758 68(2), 117-137.
759 Dixey, F. (1938). The Nyasa-Shire Rift. *The Geographical Journal*, 91(1), 51-56.
760 doi:10.2308/1787817
761 Dulanya, Z. (2017). A review of the geomorphotectonic evolution of the south Malawi rift.
762 *Journal of African Earth Sciences*, 129, 728-738.
763 http://dx.doi.org/10.1016/j.jafrearsci.2017.02.016
764 Dulanya, Z., Norales-Simfors, N., & Sivertun, Å. (2010). Comparative study of the silica and
765 cation geothermometry of the Malawi hot springs: Potential alternative energy
766 source. *Journal of African Earth Sciences*, 57(4) 321-327.
767 https://doi.org/10.1016/j.afrearsci.2009.11.001
768 Ebinger, C. J. (2005). Continental break-up: The East African perspective. *Astronomy &*
769 *Geophysics*, 46(2), 16-21. https://doi.org/10.1111/j.1468-4004.2005.46216.x
770 Ebinger, C. J., & Casey, M. (2001). Continental breakup in magmatic provinces: An Ethiopian
771 example. *Geology*, 29(6), 527-530. https://doi.org/10.1130/0091-
772 7613(2001)029<0527:CBIMPA>2.0.CO;2

773 Ebinger, C. J., Deino, A. L., Tesha, A. L., Becker, T., & Ring, U. (1993). Tectonic controls on rift
774 basin morphology: Evolution of northern Malawi (Nyasa) Rift, *Journal of Geophysical*
775 *Research: Solid Earth*, 98(B10), 17821-17836. https://doi.org/10.1029/93JB01392
776 Ebinger, C. J., Jackson, J. A., Foster, A. N., & Hayward, N. J. (1999). Extensional basin
777 geometry and the elastic lithosphere. *Philosophical Transactions of the Royal Society*
778 *A*, 357(1753), 741-765. https://doi.org/10.1098/rsta.1999.0351
779 Ebinger, C. J., Keir, D., Bastow, I. D., Whaler, K., Hammond, J. O. S., Ayele, A., Miller, M. S.,
780 Tiberi, C., & Hautot, S. (2017). Crustal structure of active deformation zones in Africa:
781 implications for global crustal processes. *Tectonics*, 36, 3298-3332.
782 https://doi.org/10.1002/2017TC004526
783 Ebinger, C. J., Oliva, S. J., Pham, T.-Q., Peterson, K., Chindandali, P., Illsley-Kemp, F., Droof,
784 C., Shillington, D. J., Accardo, N. J., Gallacher, R. J., Gaherty, J., Nyblade, A. A., &
785 Mulibo, G. (2019). Kinematics of active deformation in the Malawi rift and Rungwe
786 Volcanic Province, Africa. *Geochemistry, Geophysics, Geosystems*, 20,
787 https://doi.org/10.1029/2019GC008354.
788 Ebinger, C. J., Rosendahl, B. R., & Reynolds, D. J. (1987). Tectonic model of the Malawi rift,
789 Africa. *Tectonophysics*, 141(1-3), 215-235. https://doi.org/10.1016/0040-
790 1951(87)90187-9
791 Ebinger, C. J., & Scholz, C. A. (2012). Continental rift basins: the East African perspective. In
792 C. Busby, A. Azor (Eds), *Tectonics of Sedimentary Basins: Recent Advances* (pp. 185-
793 208). Chichester, UK: John Wiley & Sons.
794 Eby, G. N., Roden-Tice, M., Krueger, H. L., Ewing, W., Faxon, E. H., & Woolley, A. R. (1995).
795 Geochronology and cooling history of the northern part of the Chilwa Alkaline

796 Province, Malawi. *Journal of African Earth Sciences*, 20(3-4), 275-288.
797 https://doi.org/10.1016/0899-5362(95)00054-W
798 England, P., & Molnar, P. (1997). The field of crustal velocity in Asia calculated from
799 Quaternary rates of slip on faults. *Geophysical Journal International*. 130(3), 551-
800 582. https://doi.org/10.1111/j.1365-246X.1997.tb01853.x
801 Fagereng, Å. (2013). Fault segmentation, deep rift earthquakes and crustal rheology:
802 Insights from the 2009 Karonga sequence and seismicity in the Rukwa-Malawi rift
803 zone. *Tectonophyisics*, 601, 216-225. https://doi.org/10/1016/j.tecto.2013.05.012
804 Flannery, J. W., & Rosendahl, B. R. (1990). The seismic stratigraphy of Lake Malawi, Africa:
805 implications for interpreting geological processes in lacustrine rifts. *Journal of African*
806 *Earth Sciences (and the Middle East)*, 10(3), 519-548. https://doi.org/10.1016/0899-
807 5362(90)90104-M
808 Fritz, H., Abdelsalam, M., Ali, K. A., Bingen, B., Collins, A. S., Fowler, A. R., et al. (2013).
809 Orogen styles in the East African Orogen: A review of the Neoproterozoic to
810 Cambrian tectonic evolution. *Journal of African Earth Sciences*. 86, 65-106.
811 https://doi.org/10.1016/j.afrearsci.2013.06.004.
812 Gaherty, J.B., Zheng, W., Shillington, D.J., Pritchard, M.W., Henderson, S.T., Chindandali,
813 P.R.N. et al. (2019). Faulting processes during early-stage rifting: seismic and
814 geodetic analysis of the 2009-2010 Northern Malawi earthquake sequence.
815 *Geophysical Journal International*, 217, 1767-1782.
816 https://doi.org/10.1093/gji/ggz119
817 Gawthorpe, R. L., & Leeder, M. R. (2000). Tectono-sedimentary evolution of active
818 extensional basins. *Basin Research*, 12(3-4), 195-218.
819 https://doi.org/10.1111/j.1365-2117.2000.00121.x

820 Goldsworthy, M. & Jackson, J. (2001). Migration of activity with normal fault systems:
821 examples from the Quaternary of mainland Greece. *Journal of Structural Geology*,
822 23(2-3), 489-506. https://doi.org/10.1016/S0191-8141(00)00121-8
823 Heimpel, M., & Olson, P. (1996). A seismodynamical model of lithosphere deformation:
824 Development of continental and oceanic rift networks. *Journal of Geophysical*
825 *Research: Solid Earth*, 101(B7). https://doi.org/10.1029/96JB00168
826 Hellebrekers, N., Niemeijer, A. R., Fagereng, Å., Manda, B., & Mvula, R. L. S. (2019). Lower
827 crustal earthquakes in the East African Rift System: Insights from frictional properties
828 of rock samples from the Malawi rift. *Tectonophyiscs*, 767.
829 https://doi.org/10.1016/j.tecto.2019.228167
830 Hodge, M., Biggs, J., Goda, K., & Aspinall, W. (2015). Assessing infrequent large earthquakes
831 using geomorphology and geodesy: the Malawi Rift. *Natural Hazards*, 76, 1781-1806.
832 https://doi.org/10.1007/s11069-014-1572-y
833 Hodge, M., Biggs, J., Fagereng, Å., Elliot, A., Mdala, H., Mphepo, F. (2019). A semi-
834 automated algorithm to quantify scarp morphology (SPARTA): application to normal
835 faults in southern Malawi. *Solid Earth*, 10, 27-57. https://doi.org/10.5194/se-10-27-
836 2019
837 Hodge, M. Biggs, J. Fagereng, Å. Mdala, H. Wedmore, L., & Williams, J. (2020). Evidence from
838 high resolution topography for multiple earthquakes on high slip-to-length fault
839 scarps: the Bilila-Mtakataka fault, Malawi. *Tectonics*.
840 https://doi.org/10.1029/2019TC005933
841 Hodge, M., Fagereng, Å., Biggs, J., & Mdala, H. (2018). Controls on Early-Rift Geometry: New
842 Perspectives from the Bilila-Mtakataka Fault, Malawi. *Geophysical Research Letters*,
843 45. https://doi.org/10.1029/2018GL077343

844 Huismans, R. S., & Beaumont, C. (2007). Roles of lithospheric strain softening and
845 heterogeneity in determining the geometry of rifts and continental margins. In G. D.
846 Karner, G. Manatschal, L. M. Pihheiro (Eds), *Imaging, Mapping and Modelling*
847 *Continental Lithosphere Extension and Breakup* (pp. 111-138). London, UK:
848 Geological Society, London, Special Publications.
849 Huismans, R. S., Beaumont, C. (2014). Rifted continental margins: The case for depth
850 dependent extension. *Earth and Planetary Science Letters*, 407, 148-162.
851 https://doi.org/10.1016/j.epsl.2014.09.032
852 Ivory, S. J., Blome, M. W., Kking, J. W., McGlue, M. M., Cole, J. E., & Cohen , A. S. (2016).
853 Environmental change explains cichlid adaptive radiation at Lake Malawi over the
854 past 1.2 million years. *Proceedings of the National Academy of Sciences of the United*
855 *States of America*, 113(42), 11895-11900. https://doi.org/10.1073/pnas.1611028113
856 Jackson, J. A., Austrheim, H., McKenzie, D., & Priestley, K. (2004). Metastability, mechanical
857 strength, and the support of mountain belts. *Geology*, 32(7), 625-628.
858 https://doi.org/10.1130/G20397.1
859 Jackson, J., & Blenkinsop, T. (1993). The Malawi Earthquake of March 10, 1989: Deep
860 faulting with the East African Rift System. *Tectonics*, 12(5), 1131-1139.
861 https://doi.org/10.1029/93TC01064
862 Kendall, J. -M., Stuart, G. W., Ebinger, C. J., Bastow, I. D., & Keir, D. (2005). Magma-assested
863 rifting in Ethiopia. *Nature*, 433, 146-148. https://doi.org/10.1038/nature03161
864 Kinabo, B. D., Atekwana, E. A., Hogan, J. P., Modisi, M. P., Wheaton, D. D., & Kampunzu, A.
865 B. (2007). Early structural development of the Okavango rift zone, NW Botswana.
866 *Journal of African Earth Sciences*, 48(2-3), 125-136.
867 https://doi.org/10.1016/j.afrearsci.2007.02.005

868 Kolawole, F., Atekwana, E. A., Laó-Dávila, D. A., Abdelsalam, M. G., Chindandali, P. R.,
869 Salima, J., & Kalindekafe, L. (2018). Active Deformation of Malawi Rift's North Hinge
870 Zone Modulated by Reactiviation of Preexisting Precambrian Shear Zone Fabric.
871 *Tectonics*, 37, 683-704. https://doi.org/10.1002/2017TC004628
872 Kostrov, V. V. (1974). Seismic moment and energy of earthquakes, and seismic flow of rock.
873 *Physics of the Solid Earth*, 1, 13-21.
874 Laó-Dávila, D. A., Al-Salmi, H. S., Abdelsalam, M. G., & Atekwana, E. A. (2015). Hierarchical
875 segmentation of the Malawi Rift: The influence of inherited lithospheric
876 heterogeneity and kinematics in the evolution of continental rifts. *Tectonics*, 34,
877 2399-2417. https://doi.org/10.1002/2015TC003953
878 Leonard, M. (2010). Earthquake Fault Scaling: Self-Consistent Relating of Rupture Length,
879 Width, Average Displacement, and Moment Release. *Bulletin of the Seismological*
880 *Society of America*, 100(5a), 1971-1988. https://doi.org/10.1785/0120090189
881 Lloyd, R., Biggs, J., & Copley, A. (*in press)*. The decade-long Machaze-Zinave aftershock
882 sequence in the slowly straining Mozambique Rift. *Geophysical Journal International*.
883 https://doi.org/10.1093/gji/ggz033
884 Lyons, R. P., Scholz, C. A., Buoniconti, M. R., & Martin, M. R. (2011). Late Quaternary
885 stratigraphic analysis of the Lake Malawi Rift, East Africa: An integration of drill-core
886 and seismic-reflection data. *Palaeogeography, Palaeoclimatology, Palaeoecology*,
887 303(1-4), 20-37, https://doi.org/10.1016/j.palaeo.2009.04.014
888 Lyons, R. P., Scholz, C. A., Cohen, A. S., King, J. W., Brown, E. T., Ivory, S. J. et al. (2015).
889 Continuous 1.3-million-year record of East African hydroclimate, and implications for
890 patterns of evolution and biodiversity. *Proceedings of the National Academy of*

Sciences of the United States of America, 112(51), 15568-15573. https://doi.org/10.1073/pnas.1512864112

McCartney, T., & Scholz, C. A. (2016). A 1.3 million year record of synchronous faulting in the hangingwall and border fault of a half-graben in the Malawi (Nyasa) Rift. *Journal of Structural Geology*, 91, 114-129. http://dx.doi.org/10.1016/j.jsg.2016.08.012

Malawi National Statistics Office, (2018). 2018 Malawi Population & Housing Census: Preliminary Report. Government of Malawi. 55pp.

Manda, B. W., Cawood, P. A., Spencer, C. J., Prave, T., Robinson, R., & Roberts, N. M. (2019). Evolution of the Mozambique Belt in Malawi constrained by granitoid U-Pb, Sm-Nd and Lu-Hf isotopic data. *Gondwana Research*, *68*, 93-107.

Midzi, V., Hlatywayo, D. J., Chapola, L. S., Kebede, F., Atakan, K., Lombe, D. K., Turyomurugyendo, G., & Tugume, F. A. (1999). Seismic hazard assessment in Eastern and Southern Africa. *Annals of Geophysics*, 42(6), 1067-1083. https://doi.org/10.4401/ag-3770

Montgomery, D. R., & Brandon, M. T. (2002). Topographic controls on erosion rates in tectonically active mountain ranges. *Earth and Planetary Science Letters*, 201(3-4), 481-489. https://doi.org/10.1016/S0012-821X(02)00725-2

Mortimer, E. Paton, D. A., Scholz, C. A., Strecker, M. R., & Blisniuk, P. (2007). Orthogonal to oblique rifting: effect of rift basin orientation in the evolution of the North basin, Malawi Rift, East Africa. *Basin Research*, 19, 393-407. https://doi.org/10.1111/j.1365-2117.2007.00332.x

Mortimer, E., Kirstein, L., Stuart, F. M., & Strecker, M. R. (2016). Spatio-temporal trends in normal-fault segmentation recorded by low-temperature thermochronology:

914 Livingstone fault scarp, Malawi Rift, East African Rift System. *Earth and Planetary*
915 *Science Letters*, 455, 62-72. https://dx.doi.org/10.1016/j.epsl.2016.08.040
916 Muirhead, J. D., Kattenhorn, S. A., Lee, H., Mana, S., Turrin, B. D., Fischer, T. P. et al. (2016).
917 Evolution of upper crustal faulting assisted by magmatic volatile during early-stage
918 continental rift development in the East African Rift. *Geosphere*, 12(6), 1670-1700.
919 https://doi.org/10.1130/GES01375.1
920 Muirhead, J. D., Wright, L. J. M., & Scholz, C. A. (2019). Rift Evolution in regions of low
921 magma input in East Africa. *Earth and Planetary Science Letters*, 506, 332-346.
922 https://doi.org/10.1016/j.epsl.2018.11.004
923 Olive, J-A., Behn, M. D., & Malatesta, L. C. (2014). Modes of extensional faulting controlled
924 by surface processes. *Geophysical Research Letters*, 41(19),
925 https://doi.org/10.1002/2014GL061507
926 Owen, R. B., Crossley, R. Johnson, T. C., Tweddle, D., Kornfield, I., Davison, S., Eccles, D. H., &
927 Engstrom, D. E. (1990). Major low levels of Lake Malawi and their implications for
928 speciation rates in cichlid fishes. *Proceedings of the Royal Society B*, 240 (1299), 519-
929 553. https://doi.org/10.1098/rspb.1990.0052
930 Pace, B., Visini, F., Scotti, O., & Peruzza, L. (2018). Preface: Linking faults to seismic hazard
931 assessment in Europe. *Natural Hazards and Earth Systems Sciences*, 18, 1349-1350.
932 https://doi.org/10.5194/nhess-18-1349-2018
933 Philippon, M. Willingshofer, E., Sokoutis, D., Corti, G., Sani, F., Bonini, M., & Cloetingh, S.
934 (2015). Slip re-orientation in oblique rifts. *Geology*, 43(2), 147-150.
935 https://doi.org/10.1130/G36208.1Reed, C. A., Liu, K. H., Chindandali, P. R. N.,
936 Massingue, B., Mdala, H., Muamina, D., Yu, Y., & Gao, S. S. (2016). Passive rifting of
937 thick lithosphere in the southern East African Rift: Evidence from mantle transition

zone discontinuity topography. *Journal of Geophysical Research: Solid Earth*. 121(11), https://doi.org/10.1002/2016JB013131

Ring, U. (1994). The influence of pre-existing structure on the evoluation of the Cenozoic Malawi rift (East African rift system). *Tectonics*, 13(2), 313-326. https://doi.org/10.1029/93TC03188

Roberts, E. M., Stevens, N. J., O'Connor, P. M., Dirks, P. H. G. M., Gottfied, M. D., Clyde, W. C. et al. (2012). Initiation of the western branch of the East African Rift coeval with the eastern branch. *Nature Geoscience*, 5, 289-294. https://doi.org/10.1038/ngeo1432

Rotevatn, A., Jackson, C. A. L., Tvedt, A. B., Bell, R. E., & Blækkan, I. (2019). How do normal faults grow? *Journal of Structural Geology*, https://doi.org/10.1016.j.jsg.2018.08.005

Saria, E., Calais, E., Stamps, D. S., Delvaux, D., & Hartnady, C. J. H. (2014). Present-day kinematics of the East African Rift. *Journal of Geophysical Research: Solid Earth*, 119(4), 3584-3600. https://doi.org/10.1002/2013JB010901

Scholz, C. A. (1995). Deltas of Lake Malawi rift, east Africa: Seismic expression and exploration implications. *AAPG Bulletin*, 79 (11). https://doi.org/10.1306/7834DE54-1721-11D7-8645000102C1865D

Scholz, C. A., & Rosendahl, B. R. (1988). Low Lake Stands in Lakes Malawi and Tanganyika, East Africa, Delineated with Multifold Seismic Data. *Science*, 240, 1645-1648. https://doi.org/10.1126/science.240.4859.1645

Scholz, C. H., & Contreras, J. C. (1998). Mechanics of continental rift architecture. *Geology*, 26(11), 967-970. https://doi.org/10.1130/0091-7613(1998)026<0967:MOCRA>2.3.CO;2

961 Scholz, C. H., & Cowie, P. A. (1990). Determination of total strain from faulting using slip
962 measurements. *Nature*, 346, 837-839.
963 Schwanghart, W., & Scherler, D. (2014). TopoTooolbox 2 – MATLAB-based software for
964 topographic analysis and modelling in Earth surface sciences. *Earth Surface*
965 *Dynamics*, 2, 1-7. https://doi.org/10.5194/esurf-2-1-2014
966 Shillington, D. J., Gaherty, J. B., Ebinger, C. J., Scholz, C. A., Selway, K., Nyblade, A. A. et al.
967 (2016). Acquisition of a Unique Onshore/Offshore Geophysical and Geochemical
968 Dataset in the Northern Malawi (Nyasa) Rift. *Seismological Research Letters*, 87(6),
969 1406-1416. https://doi.org/10.1785/0220160112
970 Shillington, D. J., Scholz, C. A., Chindandali, P. R. N., Gaherty, J. B., Accardo, N. J., Onyango,
971 E., Ebinger, C. J., Nyblade, A. A. (2020). Controls on rift faulting in the North Basin of
972 the Malawi (Nyasa) Rift, East Africa. *Tectonics*,
973 https://doi.org'10.1029/2019TC005633
974 Specht, T. D., & Rosendahl, B. R. (1989). Architecture of the Lake Malawi Rift, East Africa.
975 *Journal of African Earth Sciences (and the Middle East)*, 8(2-4), 355-382.
976 https://doi.org/10.1016/S0899-5362(89)80032-6
977 Stamps, D. S., Saria, E., & Kreemer, C. (2018). A Geodetic Strain Rate Model for the East
978 African Rift System. *Scientific Reports*, 8, 732. https://doi.org/10.1038/s41598-017-
979 19097-w
980 Taulo, J. L., Gondwe, K. J., & Sebitosi, A. B. (2015). Energy supply in Malawi: Options and
981 issues. *Journal of Energy in Southern Africa*, 26(2) 19-32.
982 Taylor, S. K., Bull, J. M., Lamarche, G. & Barnes, P. M. (2004). Normal fault growth and
983 linkage in the Whakatane Graben, New Zealand, during the last 1.3 Myr. *Journal of*
984 *Geophysical Research: Solid Earth*, 109(B2). https://doi.org/10.1029/2003JB002412

985 Tedla, G. E., van der Meijde, M., Nyblade, A. A., & van der Meer, F. D. (2011). A crustal
986 thickness map of Africa derived from a global gravity field model using Euler
987 deconvolution. *Geophysical Journal International*, 187(1), 1-9.
988 https://doi.org/10.1111/j.1365-246X.2011.05140.x
989 Thomas, D. S. G., Bailey, R., Shaw, P. A., Durcan J. A., & Singarayer, J. S. (2009). Late
990 Quaternary highstands at Lake Chilwa, Malawi: Frequency, timing and possible
991 forcing mechanisms in the last 44 ka. *Quaternary Science Reviews*, 28, 526-539.
992 https://doi.org/10.1016/jquascirev.2008.10.023
993 Turcotte, D. L., & Schubert, G. (1982). *Geodynamics*, Wiley and Sons, New York, 456p
994 Wang, T., Feng, J., Liu, K. H., Gao, S. S. (2019). Crustal structure beneath the Malawi and
995 Luangwa Rift Zones and adjacent areas from ambient noise tomography. *Gondwana*
996 *Research*, 67, 187-198. https://doi.org/10.1016/j.gr.2018.10.018
997 Wernicke, B., & Axen, G. J. (1988). On the role of isostasy in the evolution of normal fault
998 systems. *Geology*, 16(9), 848-851. https://doi.org/10.1130/0091-
999 7613(1988)016<0848:OTROII>2.3.CO;2
1000 Wessel, B., Huber, M., Wohlfart, C., Marschalk, U., Kosmann, D., Roth, A. (2018). Accuracy
1001 assessment of the global TanDEM-X Digital Elevation Model with GPS data. *ISPRS*
1002 *Journal of Photogrammetry and Remote Sensing*, 139, 171-182.
1003 https://doi.org/10.1016/j.isprsjprs.2018.02.017
1004 Wessel, P. & Smith, W.H. (1998), New, improved version of Generic Mapping Tools released.
1005 *Eos, Transactions American Geophysical Union*, 79, 579.
1006 Wheeler, W.H., and Karson, J.A., 1989, Structure and kinematics of the Livingstone
1007 Mountains border fault zone, Nyasa (Malawi) Rift, southwestern Tanzania: Journal of
1008 African Earth Sciences (and the Middle East), v. 8, p. 393–413, doi:10.1016/S0899-

1009 5362(89)80034-X.

1010 Whittaker, A. C., Attal, M., Cowie, P. A., Tucker, G. E., & Roberts, G. (2008). Decoding
1011 temporal and spatial patterns of fault uplift using transient river long profiles.
1012 *Geomorphology*, 100 (3-4), pp 506-526. https://doi.org/j.geomorph.2008.01.018

1013 Whipple, K. X., & Tucker, G. E. (1999). Dynamics of the stream-power river incision model:
1014 Implications for height limits of mountain ranges, landscape response timescales,
1015 and research needs. *Journal of Geophysical Research: Solid Earth*, 104(B8), 17661-
1016 17674. https://doi.org/10.1029/1999JB900120

1017 Williams, J. N., Fagereng, Å., Wedmore, L. N. J., Biggs, J., Mphepo, F., Dulanya, Z., Mdala, H.,
1018 & Blenkinsop, T. (2019). How do variably striking faults reactivate during rifting?
1019 Insights from southern Malawi. *Geochemistry, Geophysics, Geosystems*,
1020 https://doi.org/10.1029/2019GC008219

1021 Wobus, C., Whipple, K. X., Kirby, E., Snyder, N., Johnson, J., Spyropolou, K. et al. (2006).
1022 Tectonics from topography: Procedures, promise and pitfalls. In S. D. Willet, N.
1023 Hovius, M. T. Brandon, & D. M. Fisher (Eds). *Tectonics, Climate and Landscape*
1024 *Evolution*, (pp. 55-74). Geological Society of America: Special Paper 398.
1025 https://doi.org/10.1130/2006.2398(04)

1026 Yu, Y., Liu, K. H., Huang, Z., Zhao, D., Reed, C. A., Moidaki, M., Lei, J., & Gao, S. S. (2017).
1027 Mantle structure beneath the incipient Okavango rift zone in southern Africa.
1028 *Geosphere*, 13(1), 102-111. https://doi.org/10.1130/GES01331.1

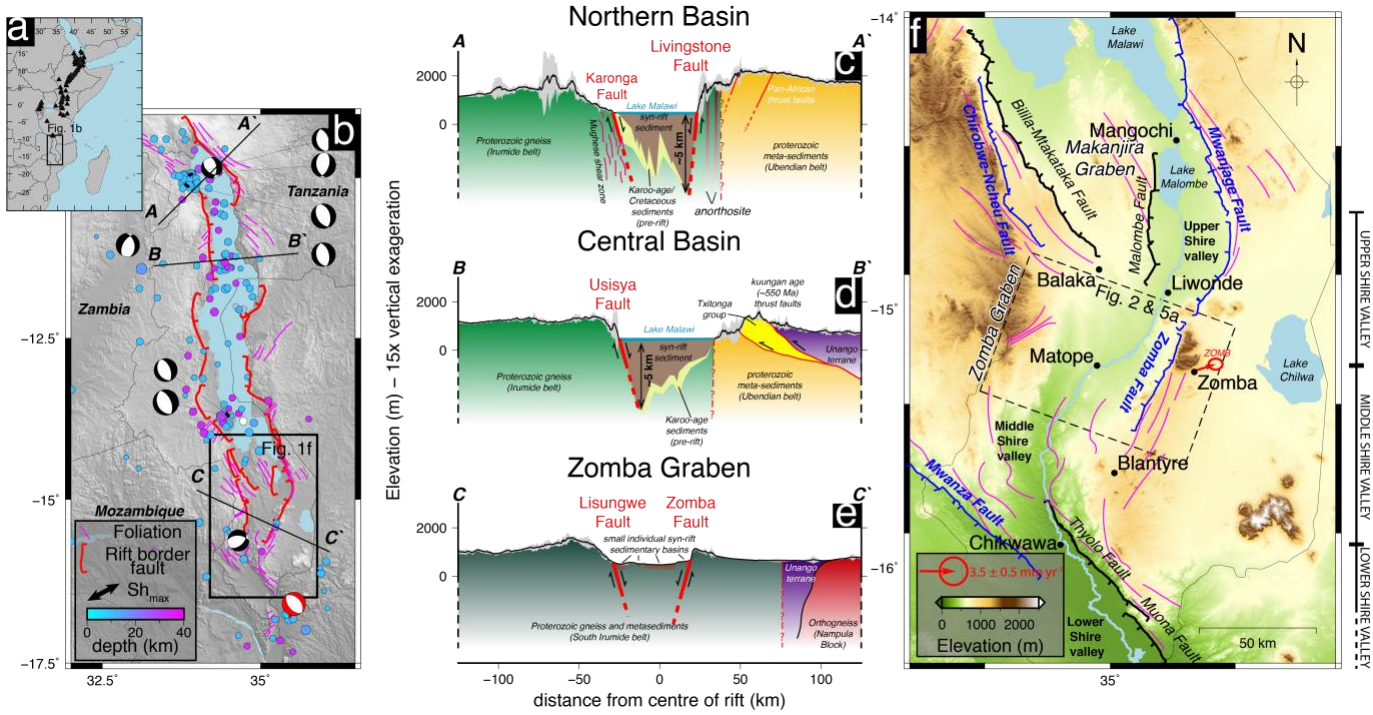

Figure 1: The location of the Zomba Graben within the East African Rift and Malawi. (a) The location of Malawi within the East African Rift. Black triangles show the active volcanoes within the rift. (b) Seismicity in the Malawi rift and the location of the Zomba Graben. Dots show National Earthquake Information Centre (NEIC) earthquakes from 1971-2018 coloured by depth. Focal mechanisms for all events greater than M_w5.0 are from Craig et al. (2010) with the exception of the red focal mechanism which shows the location and CMT mechanism of the 17th March 2018 Nsanje earthquake. The Sh_{max} direction is from Delvaux and Barth (2010). Rift border faults (in red) are adapted from Láo-Dávila et al. (2015). Foliation trend (pink lines) is adapted from Williams et al. (2019). (c-e) Crustal-scale geologic cross sections and topographic profiles showing the major border faults and sedimentary basins across the Malawi Rift. Above 0 m elevation is to scale, below 0 m elevation is not to scale. Major border faults are marked in thicker red lines. The black line is the median topography in a 5 km either side of the lines shown in part b. The grey shading represents the maximum and minimum topography in that same swath. Geology has been adapted

from Fritz et al., 2013. Basin and sediment depths for profiles a and b are adapted from Accardo et al. (2018) and Shillington et al. (2020), but intrabasin faults are not plotted. In the Zomba Graben, the thickness of hanging wall sediments is poorly constrained but boreholes have suggested thicknesses of <50 m in places (Bloomfield and Garson, 1965; see also Figure S3 and S6). Note that the nature of the boundaries between the Ubendian and Irumide belts, and the South Irumide Belt and the Unango Terrane is uncertain. (f) Overview map of southern Malawi showing the location of the Zomba Graben relative to other known faults in the region. Faults where scarps have been detected and measured are indicated in black. Faults which are suspected as active but with no measurements of throw or where no fault scarp has previously been detected are shown in blue. GPS vector relative to a stable Nubian plate is shown in red (Stamps et al., 2018). Foliation trend is shown in pink

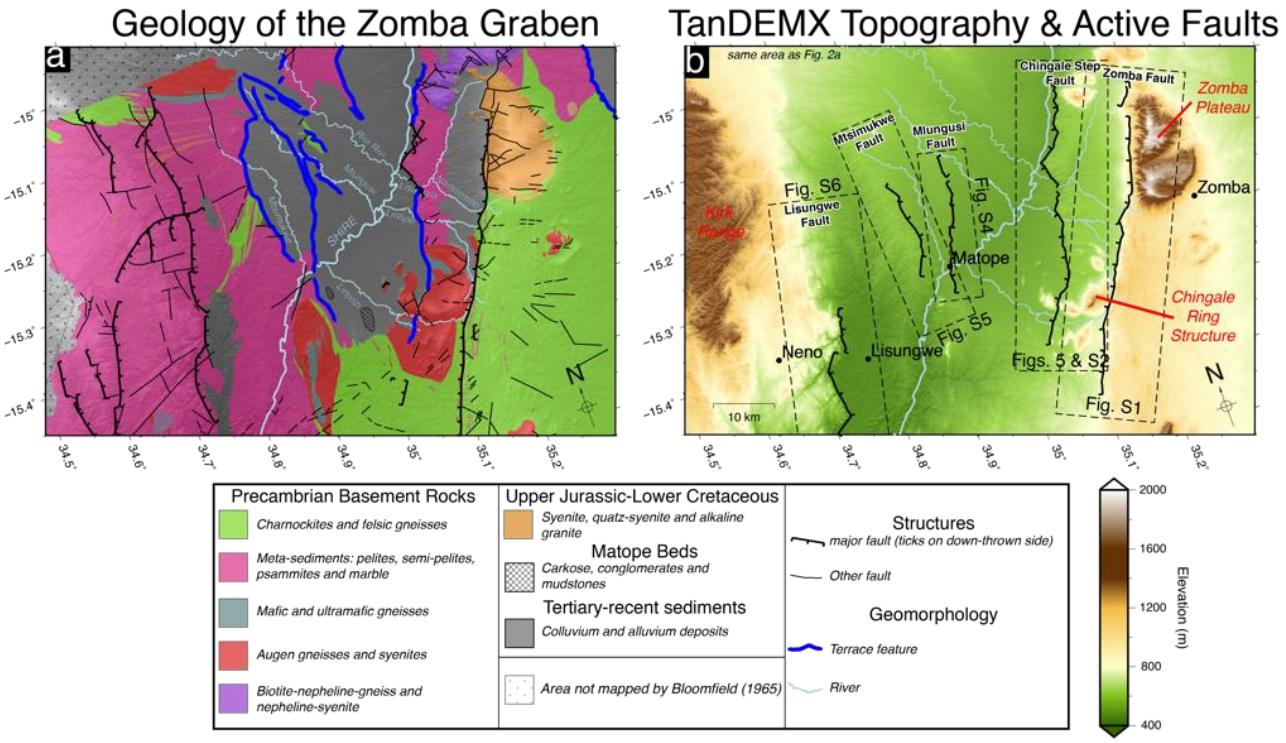

1056

1057 Figure 2: Geology and topography of the Zomba Graben. (a) Geological map of the Zomba

1058 Graben adapted from Bloomfield (1965). (b) TanDEM-X digital elevation model of the

1059 Zomba in the same area as part a. For a slope map of the same area please refer to Figure

1060 S1.

1061

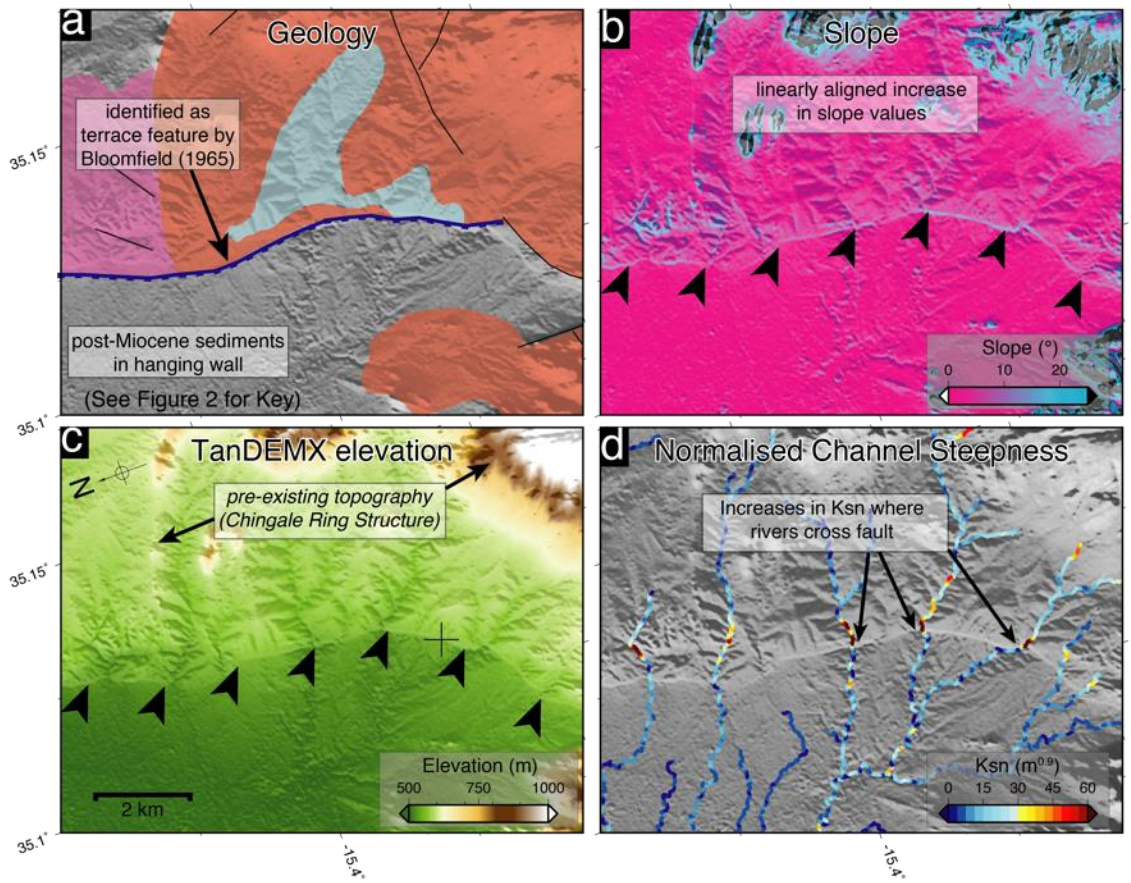

1062

1063 Figure 3: The method used to identify and measure the activity of the faults in the Zomba
1064 Graben. A small section of the Chingale Step fault is used as an example. For full details of
1065 each fault see the supplementary material. (a) Geological maps (Bloomfield, 1965) were
1066 used to identify locations where scarps or terrace features had Tertiary-recent sediments in
1067 their hanging wall. (b) Slope map that shows a linearly aligned increase in slope values that
1068 correspond to the terrace feature in part a and the increase in topography in part c. (c)
1069 TanDEM-X DEM, with the location of the fault identified by the change in elevation and
1070 indicated by the black arrows. (d) The normalised channel steepness index (K_{sn}) increases in
1071 the footwall of the fault as the river channels cross the fault.

1072

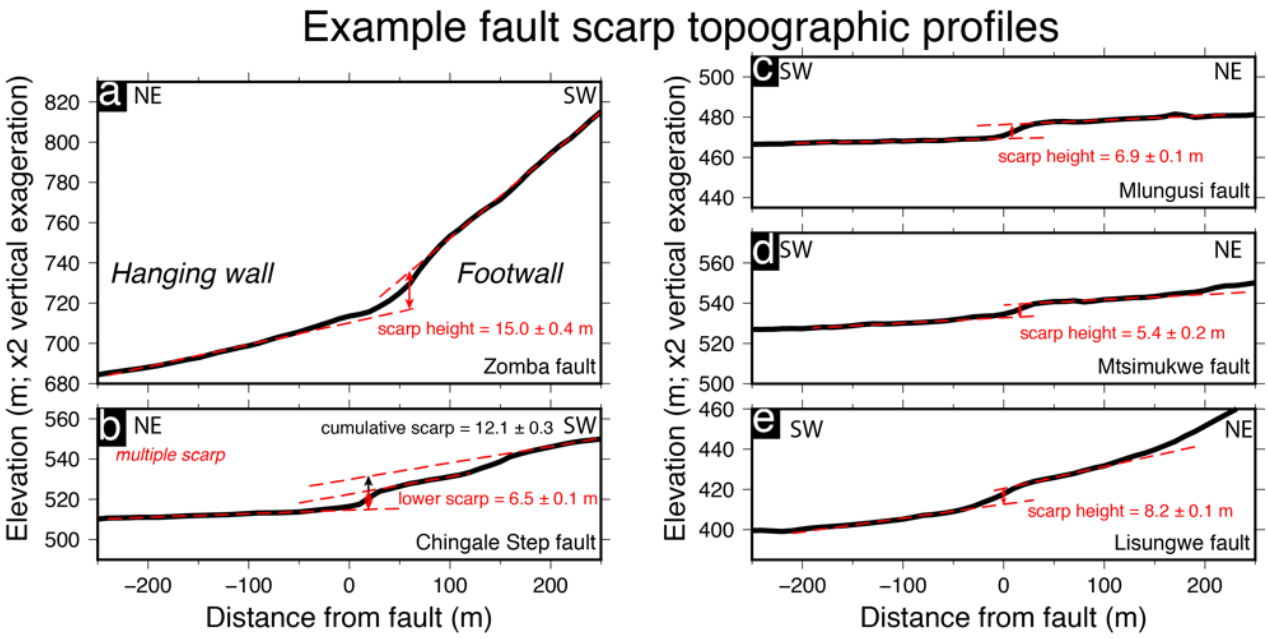

1073

1074 Figure 4: Examples of topographic profiles used to assess fault activity in the Zomba Graben.

1075 The fault scarps are characterised by locally steep slopes at the base of the larger footwall

1076 escarpments associated with faults dipping to the west (a-b) and to the east (c-e). (a)

1077 Example topographic profiles used to calculate the height of the fault scarps in the Zomba

1078 Graben. (b) Example topographic profile along the Chingale Step fault, where a multiple

1079 scarp was observed with the lower and upper slopes offset in at least two difference events.

1080 (c) Fault scarp observed along the east dipping Mlungusi fault. (d) Fault scarp observed

1081 along the Mtsimukwe fault. (e) Fault scarp observed along the Lisungwe fault.

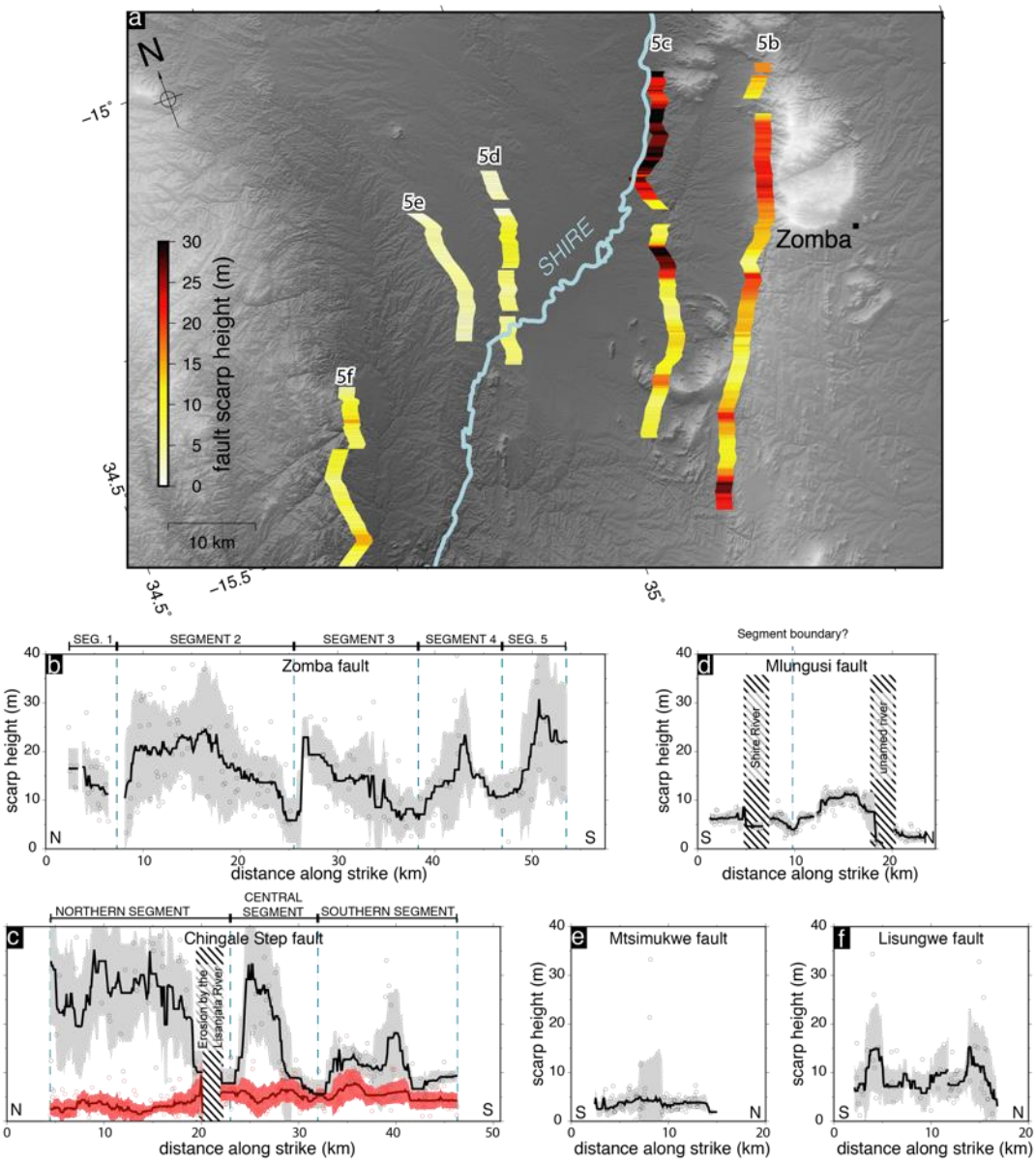

1082

1083 Figure 5: Fault scarp height for the five faults in the Zomba Graben. (a) A map of the Zomba
1084 Graben with the fault traces coloured by the 3 km moving median fault scarp height shown
1085 in parts b-f. In parts b-f horizontal and vertical axis are plotted at the same scale. The circles
1086 show the individual measurements, the solid black lines are the 3 km wide moving medians
1087 with the 1σ error shaded. The hatched areas are where offsets have been locally eroded by
1088 rivers. Inferred segment boundaries are indicated with blue dashed lines. (b) The Zomba
1089 fault oriented from north to south. (c) The Chingale Step fault oriented from north to south.
1090 The red lines and points indicate the height of the lowest scarp on the composite scarp (see

1091 Figure 3 and S3). The black line and points are the height of the composite scarp. (d) The
1092 Mlungusi fault oriented from south to north. (e) The Mtsimukwe fault oriented from south
1093 to north. (f) The Lisungwe fault oriented from south to north.

1094

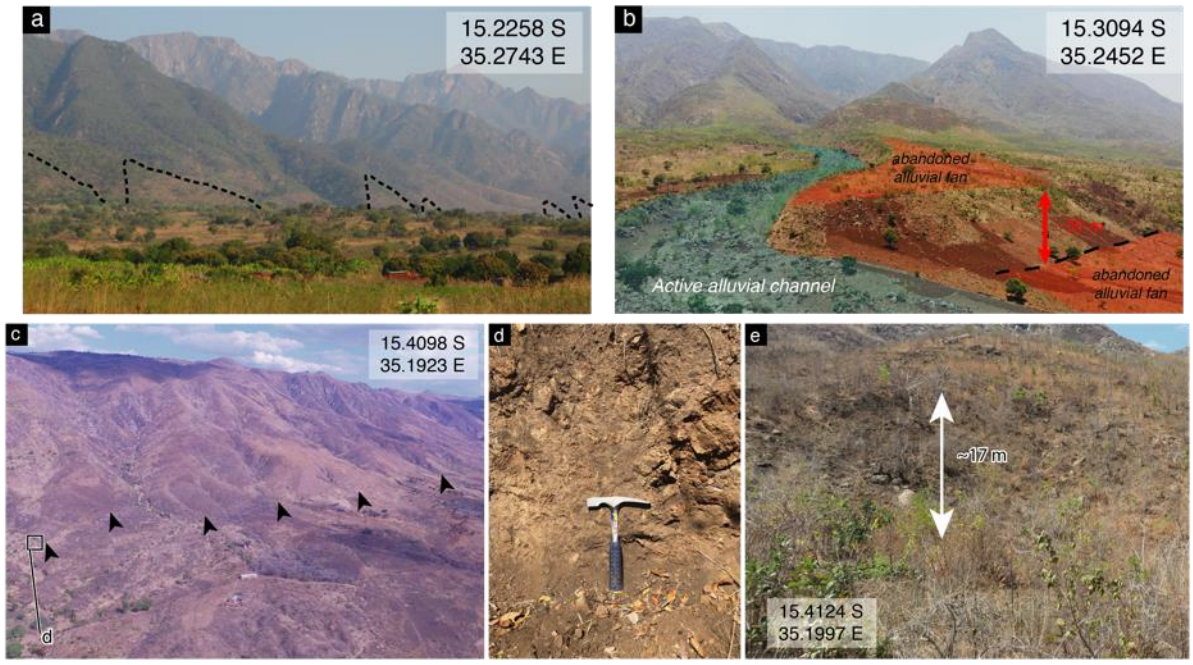

1095

1096 Figure 6: Field observations of the Zomba fault. (a) Triangular facets (black dashed lines)
1097 observed at the northern end of the fault. The hanging wall-footwall contact of the facets is
1098 not visible in this photo. (b) Alluvial fan observed in the section of the fault where the
1099 Zomba plateau is in the footwall of the fault. The age of the alluvial fan is not known. (c) The
1100 fault scarp at the southern end of the Zomba fault (indicated by black arrows). (d) Fractured
1101 basement rock consistent with a fault zone observed where exposed in stream beds at the
1102 base of the fault scarp. (e) Steep scarp at the base of the footwall escarpment. A scarp
1103 height of ~17 m was measured in the field and is consistent with the measurements made
1104 using remote sensing data (Figure 5).

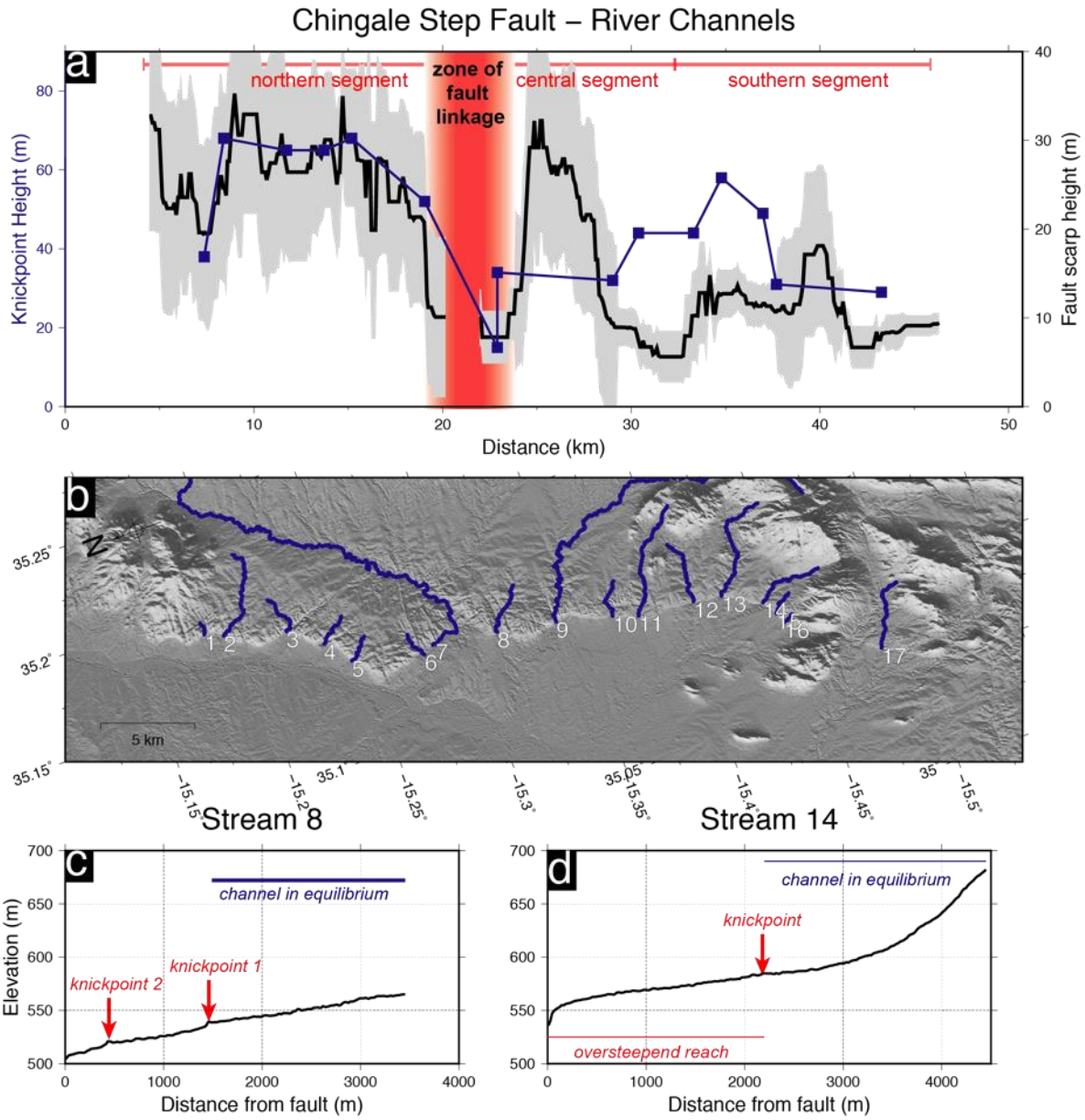

1105

1106 Figure 7: The transient response of rivers crossing the Chingale Step fault. (a) The elevation
1107 of the knickpoints, at the top of oversteepened portions of the river long profiles (see Figure
1108 S4), above the fault scarp (blue squares). The black shaded line is the fault scarp height on
1109 the Chingale Step fault (grey shading is 1 σ error). The gap is due to erosion by the Lisanjala
1110 River (stream 7). (b) Map of the footwall river channels that cross the Chingale Step fault.
1111 Channels 7 and 9 were not analysed as they both exhibit behaviour which would suggest
1112 that they were not detachment limited and both cross multiple lithologies in the footwall of

the Chingale Step fault. (c) Stream 8 which is found in the linkage zone between the northern and central segment of the fault and displays two prominent knickpoints. (d) Stream 14 shows a clear oversteepened reach in the footwall of the fault. Further upstream the channel is in equilibrium.

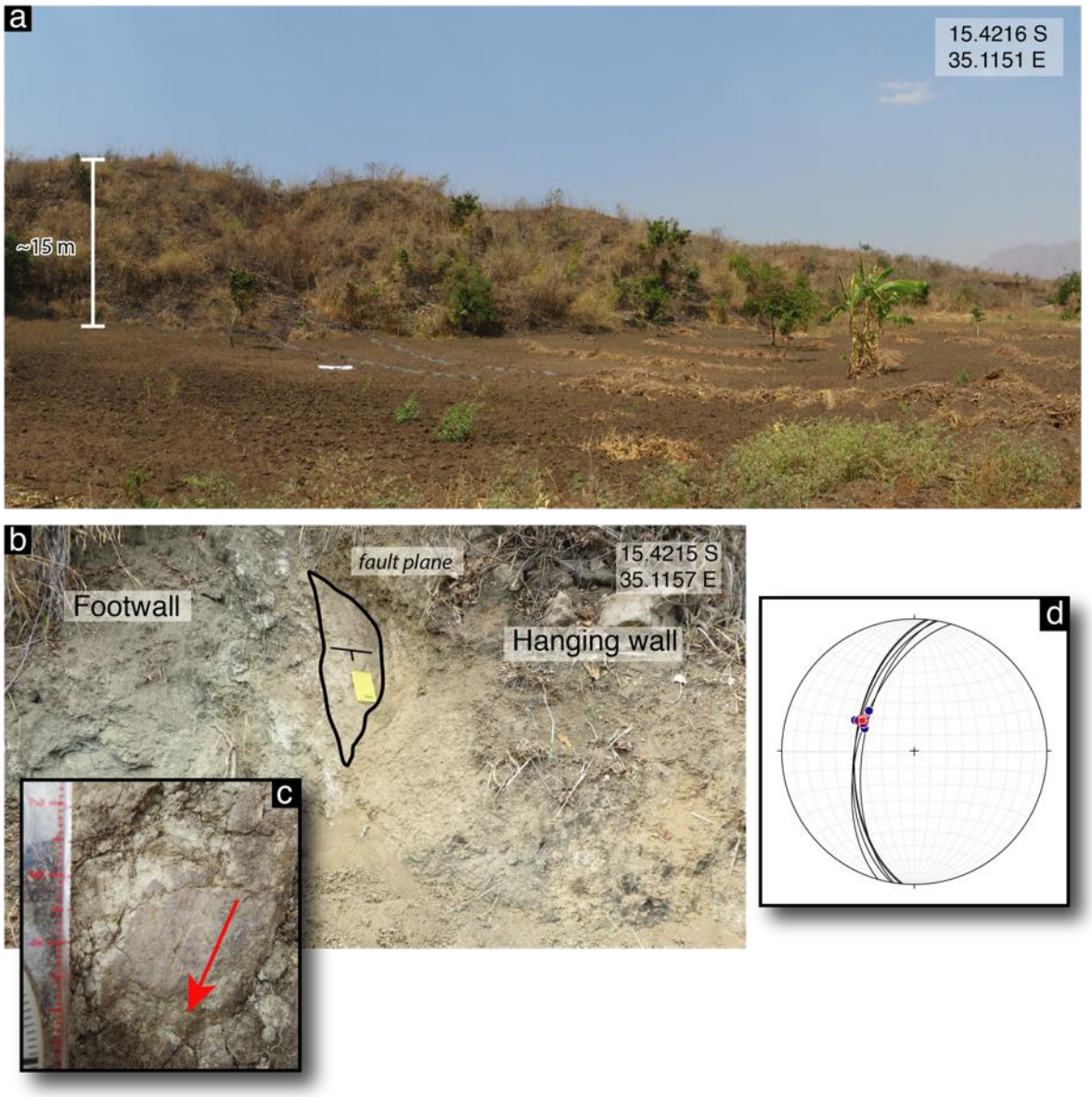

1118

1119 Figure 8. The Chingale Step fault. (a) Fault scarp along the southern section of the Chingale
1120 Step fault. The hanging wall is comprised of a mix of fluvial, alluvial and lacustrine deposits
1121 whereas bedrock is exposed in the footwall with a thin soil cover. The slickensides shown in
1122 part c were observed in a stream bed ~50 m north of this site. (b) The exposure of the fault
1123 plane at the Kalira River site. (c) Exposed slickensides measured on a polished fault plane
1124 exposed at the side of the riverbank. (d) Stereonet showing the fault plane orientation

(black lines), the average strike and dip is 189°/54°. The trend and plunge of the slickensides (blue dots) is shown in part b, the average trend and plunge (red dot) is 52° $\rightarrow$ 301° (N=5).

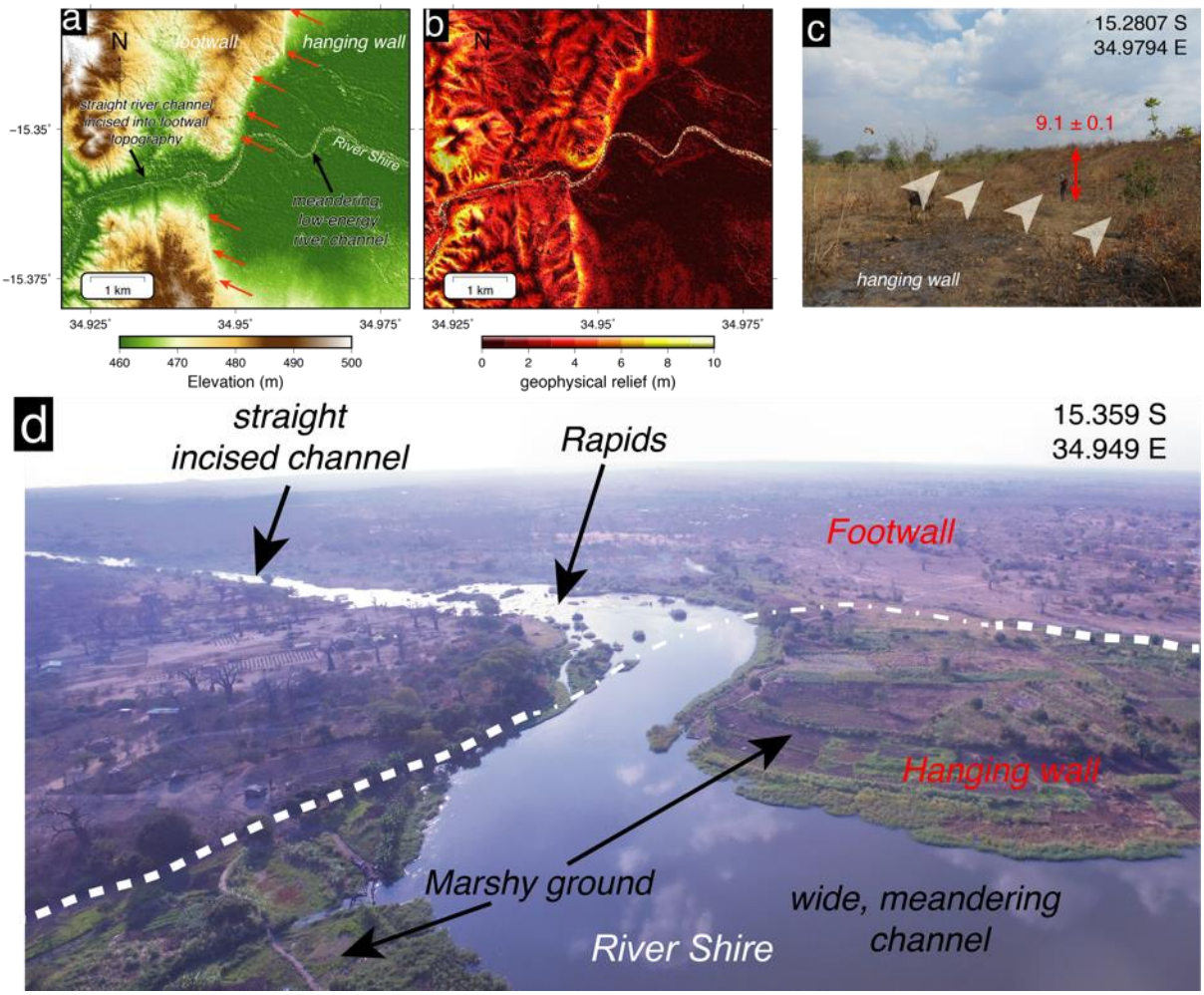

Figure 9: The interaction between the Mlungusi fault and the Shire River. (a) DEM of the location where the Shire River crosses the Mlungusi fault with the fault scarp indicated by red arrows. (b) Geophysical relief map (the difference between the elevation of each point and the maximum elevation within 200 m of each point) of the same area as part b. (c) The fault scarp formed by the Mlungusi fault (~3 km to north of parts a, b and d). The white arrows indicate the base of the fault scarp, the offset is indicated in red. (d) Photo taken from a drone of the location where the Shire River crosses the Mlungusi fault. The location of the scarp is indicated with white dashed line where it can be observed. A thinner dotted and dashed line is used where the scarp has been eroded by the Shire river and consequently the location is inferred.

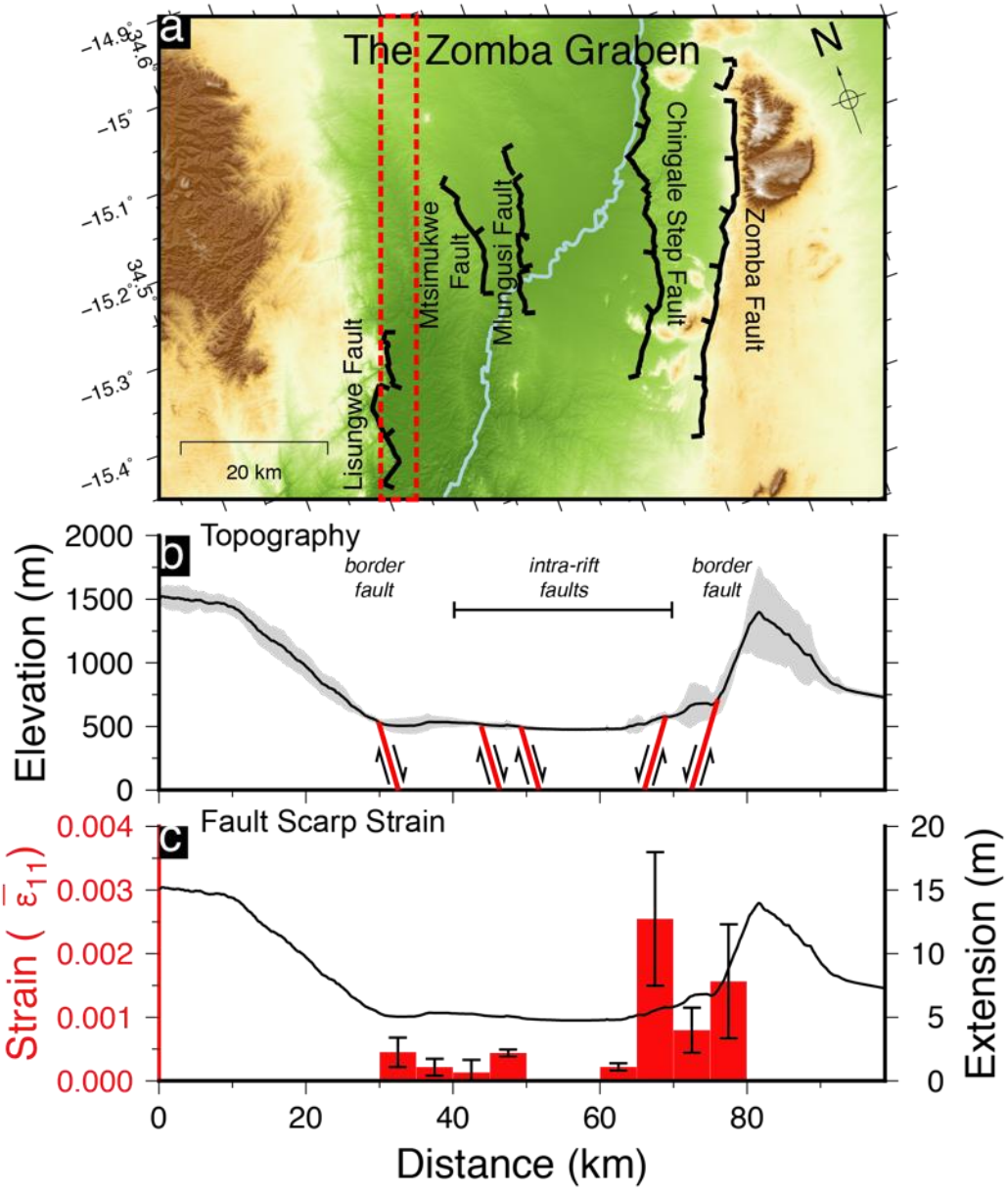

Figure 10: Distribution of strain in the Zomba Graben. (a) Active faults and topography of the Zomba Graben. The active faults analysed in this paper are indicated with thick black lines. ε_{11} direction for parts b-c is horizontal in this projection (projection is rotated 10° to the east). An example of the 5 km width bins used to calculate the strain is shown with the dotted red line. (b) Swath topography extracted 15 km either side of a horizontal line across the centre of part a. The mean topography is shown in the dark back line with 95% confidence shaded in grey. The locations of the faults are indicated by the red lines. (c) Rift-

wide distribution of strain calculated using the fault scarp offsets measured across each fault in 5km width bins. The length of the bins matches the area shown in part a. The maximum scarp height in each 5km width bin before the strain is used to calculate ε_{11}. For the Chingale Step fault, the cumulative scarp height of the multiple scarp is used, rather than the height of the lower offset measured at the base of the fault scarp.

1152 Table 1: The Geometry, activity rates and strain across faults in the Zomba Graben.

Fault	Length (km)	Strike(°)	Dip Direction	Maximum Scarp height (m)	% of late-Quaternary strain
Zomba – whole fault	51	025	West	30.8 ± 13.7	40 ± 17
Zomba – segment 1	4			16.8 ± 5.1	
Zomba – segment 2	18			24.5 ± 14.1	
Zomba – segment 3	13			22.9 ± 4.2	
Zomba – segment 4	8			23.3 ± 9.7	
Zomba – segment 5	6			30.8 ± 13.7	
Chingale Step – whole fault, cumulative scarp	39	022	West	35.3 ± 14.6	42 ± 17
Chingale Step – whole fault, lower scarp	39			9.5 ± 4.2	
Chingale Step – northern segment	18			35.3 ± 14.6	
Chingale Step – central segment	10			32.2 ±1 3.3	
Chingale Step – southern segment	14			18.1 ± 2.9	
Mlungusi	22	013	East	11.4 ± 1.4	7 ± 1
Mtsimukwe	13	177	East	14.6 ± 8.4	6 ± 6
Lisungwe	23	019	East	15.3 ± 7.8	6 ± 3

1153